# 6

# OTHER ADVANCED TRANSMISSION LINES

## 6.1 INTRODUCTION

This chapter is focused on advanced topics not covered in the previous chapters, namely, magnetoinductive-wave (MIW) and electroinductive-wave (EIW) delay lines, differential transmission lines with common-mode suppression, wideband artificial transmission lines (including CRLH lines based on the lattice network unit cell and active—non-Foster—transmission lines), and substrate-integrated waveguides (SIWs). Rather than an in-depth treatment of each of these lines (all of them can be the subject of an intensive analysis), the aim of the chapter is to briefly analyze the main properties of such lines, their advantages, and some applications.

## 6.2 MAGNETOINDUCTIVE-WAVE AND ELECTROINDUCTIVE-WAVE DELAY LINES

MIW and EIW delay lines are waveguiding structures consisting of chains of coupled resonant elements that typically exhibit very small phase and group velocities. These lines can be an alternative to surface acoustic waves or ferrite-based lines as delay lines, as long as slow wave factors as high as $c/v_g \sim 100$ can be achieved. Although this value is not comparable to those achievable in surface acoustic or ferrite delay lines, the main advantage of MIW and EIW lines is their simple design/fabrication process, since these lines can be implemented in standard printed circuit boards (PCBs). Moreover, due to

*Artificial Transmission Lines for RF and Microwave Applications*, First Edition. Ferran Martín.

the scalability of planar circuits, MIW and EIW lines can be designed to be operative over a very wide frequency band of the microwave spectrum.

### 6.2.1 Dispersion Characteristics

The properties and dispersion characteristics of waves in magnetically coupled capacitively loaded loops were first studied by the group of Prof. Solymar in 2002 [1, 2]. Following these pioneering works, the same group published several papers on the topic of MIWs devoted to experimentally verify the dispersion characteristics [3], to highlight some potential applications (i.e., dividers and couplers) [4], and to study the interaction between MIWs and electromagnetic (EM) waves [5]. In 2004, it was demonstrated that MIWs can be supported by a chain of SRRs printed on a microwave substrate [6]. Indeed, MIWs are expected to be present in whatever periodic structure where the elements are magnetically coupled.

Without loss of generality, let us consider from now on MIW lines based on SRRs. Although, MIWs can be supported in one-dimensional chains of axially oriented or coplanar arranged SRRs (Fig. 6.1), the interest from the point of view of planar waveguiding structures is in the coplanar configuration. The dispersion relation in any of the structures of Figure 6.1 can be easily inferred from the circuit model of the unit cell, depicted in Figure 6.2a. $L$ and $C$ are the inductance and capacitance of the SRRs and $M$ is the mutual inductance between adjacent SRRs (the first neighbor approximation is considered). The circuit model of Figure 6.2a can be transformed to

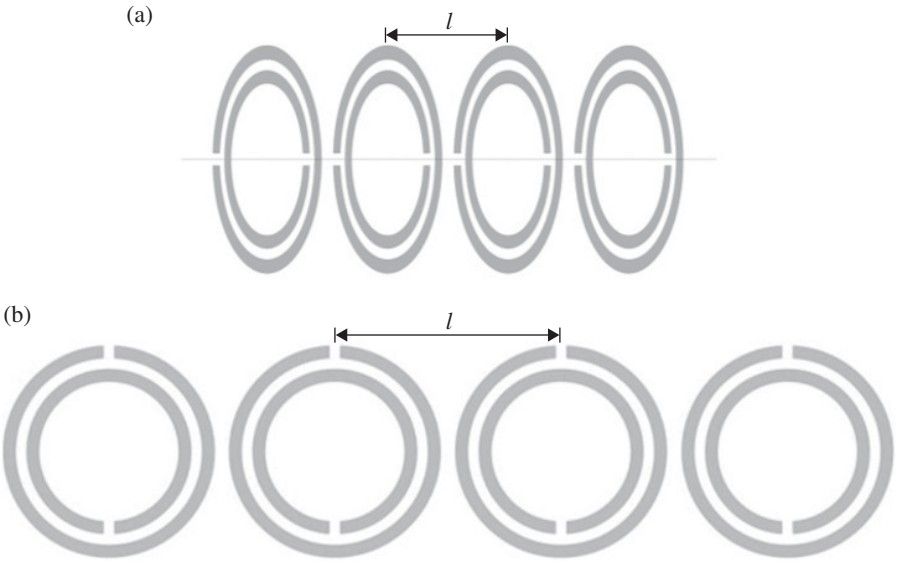


**FIGURE 6.1** One-dimensional chain of inductively coupled SRRs. (a) Axial configuration and (b) coplanar configuration.

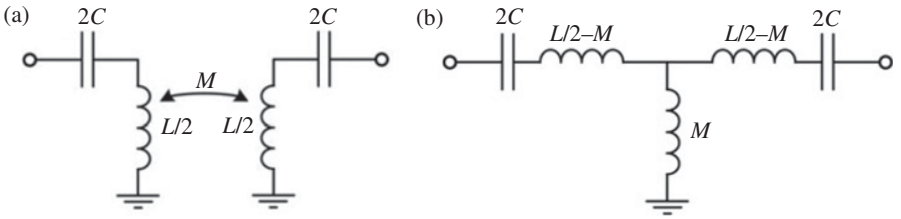


**FIGURE 6.2** (a) Equivalent circuit model (unit cell) of the chain of SRRs of Figure 1, and (b) transformed model.

the T-circuit shown in Figure 6.2b. Application of expression (2.33) gives the dispersion relation, which is usually written as follows:

$$\frac{\omega_o^2}{\omega^2} = 1 \pm \frac{2|M|}{L}\cos(\beta l) \tag{6.1}$$

where

$$\omega_o = \frac{1}{\sqrt{LC}} \tag{6.2}$$

and the + and − sign corresponds to the axial and coplanar configuration, respectively. The difference arises from the different sign of the mutual inductance for the axial (positive) and coplanar (negative) configurations. According to (6.1), wave propagation is backward in the coplanar configuration, whereas it is forward for axially oriented SRRs. Notice that the limits of the transmission band are given by the frequencies

$$\omega_{\pm} = \frac{\omega_o}{\sqrt{1 \mp \dfrac{2|M|}{L}}} \tag{6.3}$$

Since the mutual inductance $M$ is typically small as compared to the inductance $L$ of the SRRs, the transmission band in MIW delay lines is very narrow, and the group velocity is very small.

By applying duality, it follows that a chain of closely located coupled complementary split-ring resonators or CSRRs (Fig. 6.3) can support electroinductive waves (EIWs) [7] (notice however that wave propagation in chains of electrically coupled resonators was already pointed out in the sixties [8]). In this case, the unit cell can be described by the circuit model depicted in Figure 6.4, which is indeed the circuit dual of the circuit model (unit cell) of the MIW delay line. In the model, $C_M$ is the mutual capacitance between adjacent CSRRs, $L_c$ is the inductance of the CSRR and the capacitance $C_G = C_c - 2C_M$, $C_c$ being the capacitance of an isolated CSRR.

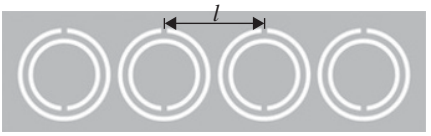


**FIGURE 6.3** One-dimensional chain of electrically coupled CSRRs, acting as an EIW delay line.

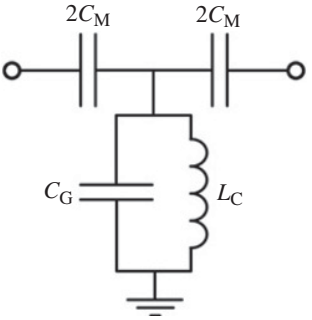


**FIGURE 6.4** Equivalent circuit model (unit cell) of the chain of CSRRs of Figure 6.3.

In this case, the dispersion relation (under the first neighbor approximation) is found to be[1]:

$$\frac{\omega_o^2}{\omega^2} = 1 - \frac{2C_M}{C_c}\cos(\beta l) \tag{6.4}$$

where

$$\omega_o = \frac{1}{\sqrt{L_c(C_G + 2C_M)}} = \frac{1}{\sqrt{L_c C_c}} \tag{6.5}$$

The backward propagation band is delimited by the frequencies given by

$$\omega_{\pm} = \frac{\omega_o}{\sqrt{1 \mp \dfrac{2C_M}{C_c}}} \tag{6.6}$$

and bandwidth broadens as the electric coupling between adjacent CSRRs increases.

The dual behavior of SRR-based MIW (coplanar configuration) and CSRR-based EIW lines is apparent by comparing (6.4–6.6) with (6.1–6.3). Notice that the

[1] In Ref. [7], the dispersion relation of CSRR-based EIW lines is presented in a different form. However, both expressions are identical. As given earlier, (6.4) is formally identical to (6.1).

dispersion relations of both lines (considering the coplanar configuration of SRRs) and bandwidth are identical as long as $|M|/L = C_M/C_c$, as expected from duality considerations.

### 6.2.2 Applications: Delay Lines and Time-Domain Reflectometry-Based Chipless Tags for RFID

As long as MIW and EIW lines are waveguiding structures, microwave devices such as couplers, dividers, phase shifters, and so on, based on such lines can be implemented [3, 4, 9, 10]. However, probably the most relevant advantage of MIW and EIW lines is the possibility to achieve very high slow-wave factors in conventional fully planar technology (i.e., PCB technology). These lines are therefore interesting as delay lines [6], and for applications requiring delay lines with significant group delay. One of such applications is the implementation of passive chipless tags for radiofrequency identification (RFID) based on time-domain reflectrometry (TDR) [11].[2]

The tags are implemented with MIW delay lines comprising a periodic array of coupled square split-ring resonators (SSRRs) [11]. Tag encoding is achieved by introducing reflectors (which provide the identification signature) between the elements of the array. When the tags are interrogated with a pulse in time domain, they produce replicas at the positions where the reflectors are placed. Thanks to the slow group velocity of the MIW delay line, the replicas of the original pulse are not overlapped in time domain and can be demodulated, thus providing the identification code of the tag. First attempts to implement TDR-based chipless tags made use of left-handed (LH) lines [12, 13]. Such lines can be designed to exhibit small group velocities, but it is not possible to achieve slow-wave factors above 10. Thus, MIW-based lines appear to be a good alternative to LH lines for the implementation of chipless tags based on delay lines. The sketch of the proposed chipless RFID system is depicted in Figure 6.5. The printed antenna is used to communicate with the reader. The reflectors are simply strips located within the MIW delay line, as depicted in Figure 6.5.

In order to design the MIW delay lines for the chipless tags, it is necessary to compute the relation between the number of bits that can be stored and the physical parameters of the lines. The number of bits that can be stored in a delay line is

$$n_b = \frac{\Delta\tau}{\tau} \tag{6.7}$$

where $\Delta\tau$ is the total delay of the line working in reflection and $\tau$ is the temporal width of the pulse sent by the reader. The pulse width depends on the bandwidth of the system. In order to compute the total delay introduced by the MIW lines, the group velocity, given by

[2] TDR-based chipless RFID tags are an alternative to the RF bar codes considered in Chapter 4. The main difference is that RF bar codes operate in the frequency domain and require large bandwidths; whereas in TDR-based chipless tags, the ID code is inferred from the echoes of a pulse in time domain.

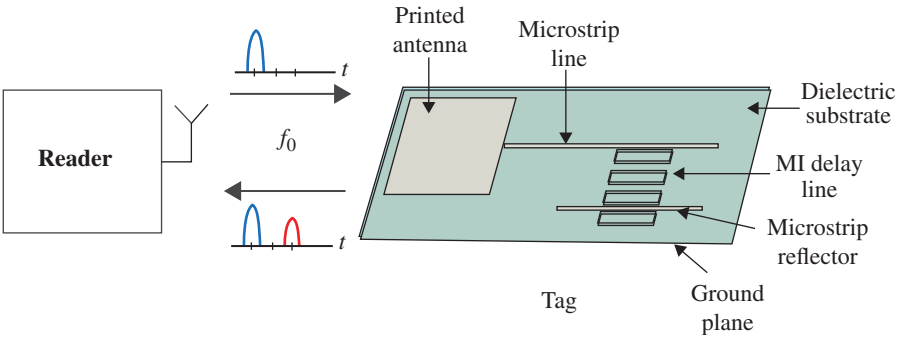


**FIGURE 6.5** Sketch of the chipless RFID system proposed in [11]. Reprinted with permission from Ref. [11]; copyright 2012 IEEE.

$$v_g = \left(\frac{\partial\beta}{\partial\omega}\right)^{-1} = l\frac{|M|}{L}\frac{\omega^3}{\omega_o^2}\sqrt{1-\left[\frac{L}{2|M|}\left(\frac{\omega_o^2}{\omega^2}-1\right)\right]^2} \tag{6.8}$$

can be approximated by its value at the central operation frequency of the system, $\omega_o$. Thus, the total delay is obtained as

$$\Delta\tau = 2\frac{n_{SSRR}l}{v_g|_{\omega_o}} = \frac{2L}{|M|}\frac{n_{SSRR}}{\omega_o} \tag{6.9}$$

where $n_{SSRR}$ is the number of SSRRs of the MIW delay line. Introducing (6.9) in (6.7), the number of bits is found to be

$$n_b = 2\frac{n_{SSRR}l}{v_g|_{\omega_o}\tau} = \frac{2L}{|M|}\frac{n_{SSRR}}{\omega_o\tau} \tag{6.10}$$

and it increases with the number of SSRRs (as expected). However, it is desirable to use the smallest possible number of SSRRs, for a certain number of bits, in order to minimize tag dimensions. Since the central operation frequency and bandwidth are fixed by design or regulatory constraints, $\tau$ and $L$ are not design parameters.[3] Thus, the only variable that can be modified in order to increment the number of bits is the mutual inductance, $M$, between the SRRs. This variable can be controlled by the separation between adjacent resonators. If this separation increases, the mutual inductance is reduced and, thus, the number of bits also increases. However, the distance

[3] The central frequency (6.2) is fixed by the inductance, $L$, and the edge capacitance of the SRRs, $C$, which is in turn given by the per-unit-length capacitance, $C_{pul}$. Usually, the per-unit-length capacitance is limited by fabrication restrictions, and the inductance is the only degree of freedom to adjust the central operation frequency, $f_0$. Thus, the inductance of the SRRs is fixed once these elements are designed to resonate at the central operation frequency.

between adjacent SSRRs is limited by three main reasons. First of all, the length of the delay line increases with the inter-SSRR distance, which is contrary to tag miniaturization. The second reason is that if the separation between SSRRs increases, the MIW bandwidth is reduced (see expression 6.3). The final one is due to propagation losses, which increase with the distance between adjacent resonators since they are intimately related to the coupling between resonators. In conclusion, a trade-off between the number of bits, line length, bandwidth, and losses, by choosing the appropriate line period, $l$, is necessary.

Figure 6.6 depicts the 2-bit chipless tags designed in Ref. [11] according to the aforementioned considerations. The distance between adjacent SRR is $l = 3.75$ mm since this represents a good trade-off between delay (16 ns), losses (5.6 dB), bandwidth (5.13%), and the total length of the line. The central frequency was chosen at $f_o = 2.45$ GHz (ISM band), and SSRRs dimensions are given in Figure 6.7. Notice that the number of bits ($n_b = 2$) is the value that results from (6.7) by considering a

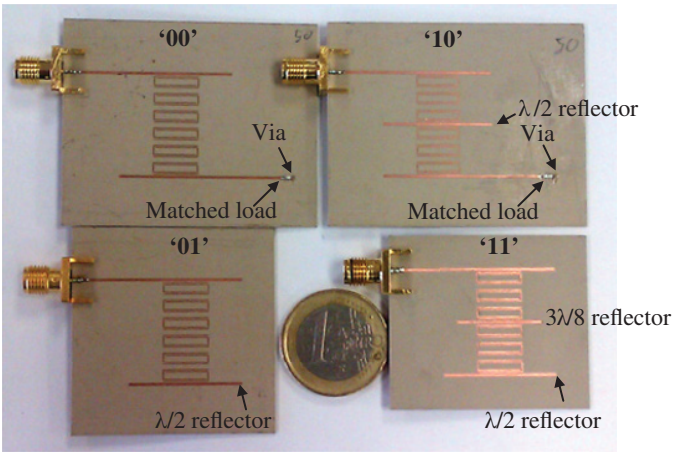


**FIGURE 6.6** Photograph of the set of 2-bit chipless tags (the antenna is not included). Reprinted with permission from Ref. [11]; copyright 2012 IEEE.

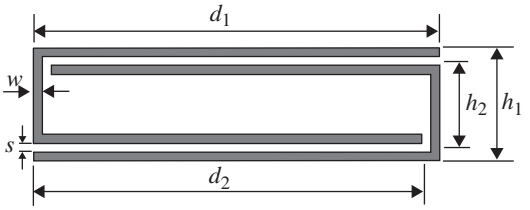


**FIGURE 6.7** Geometry of the SSRR and relevant dimensions ($d_1 = 9.6$ mm, $h_1 = 2.6$ mm, and $s = w = 0.20$ mm). The substrate is the *Rogers RO3010* with dielectric constant $\varepsilon_r = 10.2$ and thickness $h = 635$ μm). Reprinted with permission from Ref. [11]; copyright 2012 IEEE.

pulse width of $\tau = 15$ ns (see Ref. [11] for more details). To avoid reflections at the end of the MIW line, which is necessary when the second bit is "0," a microstrip line ended with a matched load was coupled at the end of the MIW delay line. As mentioned earlier, the proposed approach to produce reflections consists of using open-ended 50-Ω microstrip lines placed between the SSRRs. For the case of the 2-bit tags, the first bit reflector is placed in the middle of the MIW delay line (between the third and fourth SSRRs in this implementation) and the second bit reflector is placed at the end of the line. When a total reflection is needed, the line acting as reflector must have a length of $\lambda/2$ at $f_0$. This is the situation when no more partial reflections are used (e.g., at the end of the line). In this case, the $\lambda/2$ lines provide a $\rho = -1$ reflection coefficient in the delay line, since the distance between the open ends and the center of the line is $\lambda/4$. If only a partial reflection is needed, the length of the reflector is made smaller, and only part of the signal is reflected back to the source. The transmitted signal may thus impinge on the additional reflectors if they are present.

Figure 6.8 shows the proposed setup to characterize the chipless tags and obtain their temporal responses. In this scheme, the generator sends a modulated Gaussian pulse at the central frequency of the system ($f_0 = 2.45$ GHz). After that, the modulated signal is transferred to the chipless tag and its response is obtained through the circulator. The output of the system is the envelope of the signal reflected back by the tag. The four tags were simulated by means of *Agilent ADS Momentum* and their temporal responses were obtained using the proposed setup in a transient simulation of *Agilent ADS*. Figure 6.9a shows the temporal response of the four tags. There are pulses at three different times. In all cases, an initial pulse is observed. This is due to certain mismatch at the tag input, so that part of the input signal is reflected back to the envelope detector without being transmitted to the tags. The second group of pulses is obtained after 16 ns approximately, which corresponds to the first identification bit. Finally, the third group of pulses is observed after 32 ns which is the total delay introduced by the MIW delay lines. These pulses correspond to the second bit. Considering −15 dB as the decision threshold, the four different possible codes ("00", "01", "10," and "11") are obtained.

The four fabricated tags were measured by means of a network analyzer. Then, their temporal responses were obtained through the *Agilent ADS* scheme proposed

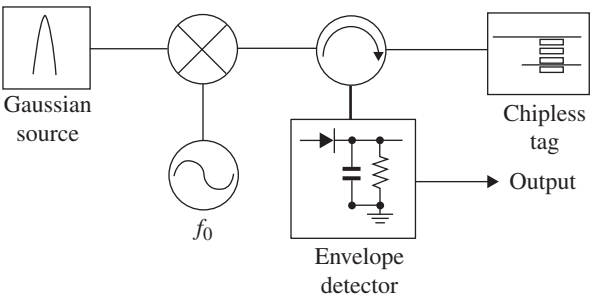


**FIGURE 6.8** Setup to obtain the temporal response of the chipless tags. Reprinted with permission from Ref. [11]; copyright 2012 IEEE.

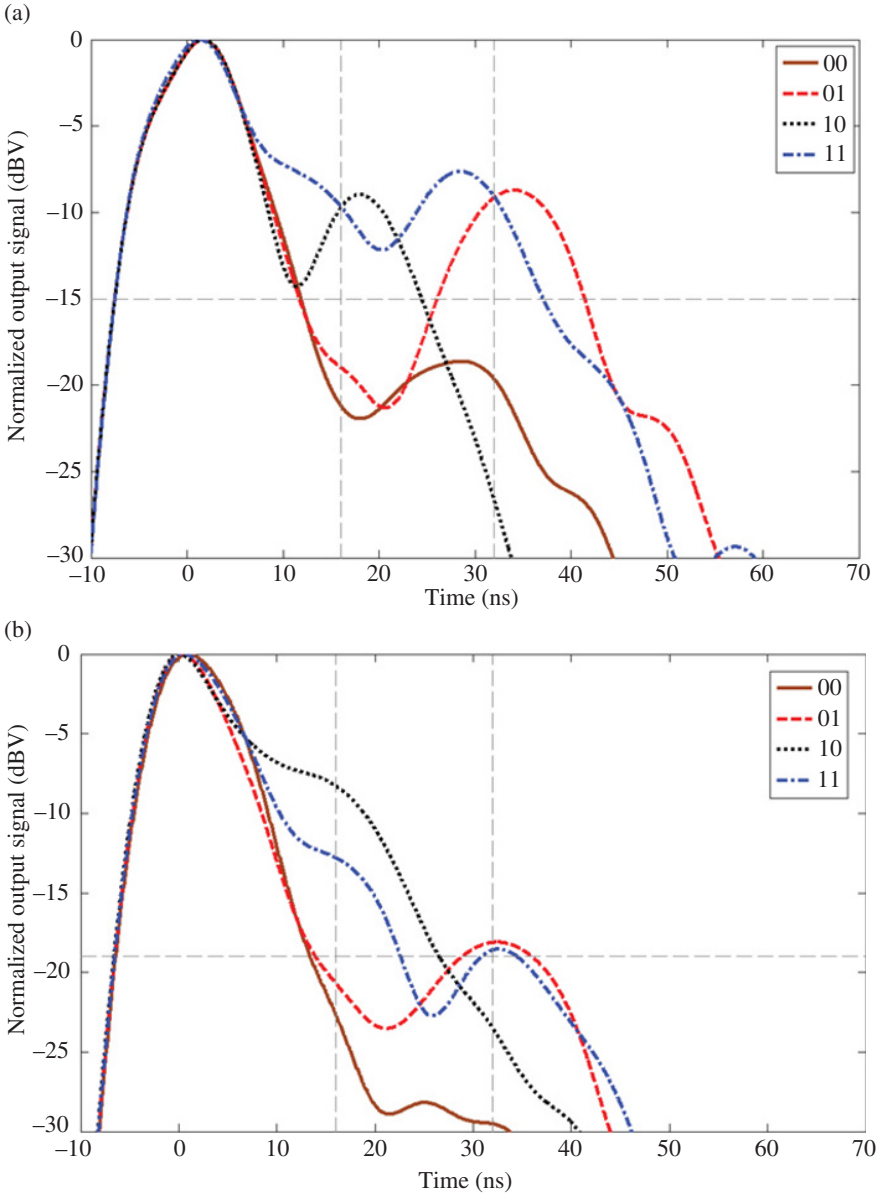


**FIGURE 6.9** Temporal response of the tags. (a) Response inferred from simulation and (b) response inferred from the fabricated tags. Reprinted with permission from Ref. [11]; copyright 2012 IEEE.

in Figure 6.8 (see Fig. 6.9b). The output signals present a similar shape, although the insertion losses in the prototypes are higher than those predicted by the simulator. Hence, the detected power corresponding to the second bit is smaller because the propagation path is twice that of the first-bit path. Nevertheless, the groups of pulses

corresponding to the first and second bits can be clearly identified at 16 ns and 32 ns, respectively. In this case, the decision threshold has been reduced to −19 dB. Considering this threshold, the four tags can be identified properly.

As compared to RF bar codes (see Subsection 4.3.2.3), TDR chipless tags based on MIW delay lines occupy much less bandwidth. However, very long delay lines are necessary to store a large amount of information, since the number of bits in TDR-based tags is proportional to the delay time.

## 6.3 BALANCED TRANSMISSION LINES WITH COMMON-MODE SUPPRESSION

Balanced (or differential) lines are of interest as interconnecting lines in high-speed digital and analog circuits due to their high immunity to environmental noise, electromagnetic interference (EMI), and crosstalk. However, in practical balanced systems, the presence of some level of common-mode noise is unavoidable. Therefore, the design of balanced lines able to suppress the common mode over a wide band, keeping the differential signals unaltered, has been a subject of interest in recent years. In this section, some strategies for common-mode noise rejection, with special emphasis on microstrip differential lines loaded with CSRRs are reviewed. A method for the design of common-mode filters based on CSRRs is proposed and used for the improvement of common-mode noise rejection in a differential bandpass filter. Finally, some examples of differential filters with inherent common-mode noise rejection are presented.

### 6.3.1 Strategies for Common-Mode Suppression

Several strategies to efficiently suppress the common mode while keeping the integrity of the differential signals in differential transmission lines have been reported [14–20]. The key idea to selectively suppress the common mode in the microwave domain is to load (or perturb) the differential line with elements acting as an efficient stopband filter for the common mode and, simultaneously, as an all-pass structure for the differential-mode in the frequency region of interest. According to Subsection 4.3.2, a transmission line loaded with a symmetric resonator with its symmetry plane aligned to that of the line is able to inhibit signal propagation (in the vicinity of resonance) if both symmetry planes are of the same EM nature. Conversely, if such planes are aligned and are of different EM nature, the line is transparent. According to the previous words, it follows that by symmetrically loading a differential microstrip line with symmetric resonators exhibiting a magnetic wall in its symmetry plane, selective mode suppression can be achieved. The reason is that the differential line exhibits a magnetic wall in its symmetry plane for the even mode, and an electric wall for the odd mode. Therefore, it is expected that the line loaded with such resonators is transparent for the differential mode and acts as a stopband filter for the common mode.

The common-mode filters based on low temperature co-fired ceramic (LTCC) technology reported in Ref. [14] or the negative permeability structures of Ref. [15] are compact and provide efficient common-mode rejection over wide frequency bands,

but they are technologically complex since multilayer structures are considered in those designs. The common-mode suppression approaches reported here are limited to two types of defect ground structures in microstrip differential lines: dumbbell-shaped resonators [16] and CSRRs [18]. It is also remarkable the strategy reported in Ref. [20], where the ground plane is structured with capacitive patches and meandered inductors that effectively act as shunt-connected series resonators for the common mode, providing lowpass filtering functionality for that mode, and all-pass behavior for the differential mode.

***6.3.1.1 Differential Lines Loaded with Dumbbell-Shaped Slotted Resonators*** Slotted dumbbell resonators symmetrically etched in the ground plane of a microstrip line can be modeled to a first-order approximation as series-connected parallel resonators [21]. These resonators are thus able to inhibit signal propagation in the vicinity of resonance. The symmetry plane of the line and resonator are magnetic walls, and this gives another interpretation to the stopband functionality of these lines, according to symmetry considerations (see earlier text). However, by symmetrically etching slotted dumbbell resonators in a differential microstrip line, it is expected that the common mode is efficiently suppressed, while signal propagation for the differential mode is preserved. In Ref. [16], the authors claim that the resonant elements open the return current path through the ground plane for the common mode, whereas the presence of resonators has small effect on the differential signals since relatively small current density returns through the ground plane for such signals. Regardless of the specific interpretation for selective common-mode suppression in differential lines loaded with slotted dumbbell resonators, such structures behave as efficient common-mode filters. Figure 6.10 depicts a specific common-mode filter topology and the frequency response. The structure is able to efficiently suppress the common-mode noise with broad stopband in the GHz range (Fig. 6.10b), yet keeping good signal integrity performance for the differential signals. In addition, mode conversion from differential-mode to common-mode, also shown in the figure, is very small.

***6.3.1.2 Differential Lines Loaded with CSRRs*** CSRRs also exhibit a magnetic wall at their symmetry plane for the fundamental resonance. Therefore by aligning this symmetry plane with the symmetry plane of the differential microstrip line, common-mode suppression and preservation of signal integrity for the differential-mode are also expected. Notice that for the differential mode, there is not a net axial electric field in the inner metallic region of the CSRR able to excite the resonators, unless symmetry is truncated. Conversely, for the common mode the electric field below the transmission lines is co-directional, and the CSRRs are excited by this mode.

As discussed in Refs [18, 19], common-mode suppression bandwidth can be enhanced by tightly coupling the resonant elements.[4] Moreover, in order to enhance the rejection bandwidth (common mode) of an individual resonator, it is necessary to increase the coupling capacitance between the pair of lines and the CSRR, and to decrease the inductance and capacitance of the CSRR. This was achieved in [18] by increasing the rings width and

[4] Square-shaped or rectangular CSRR geometries favor interresonator coupling.

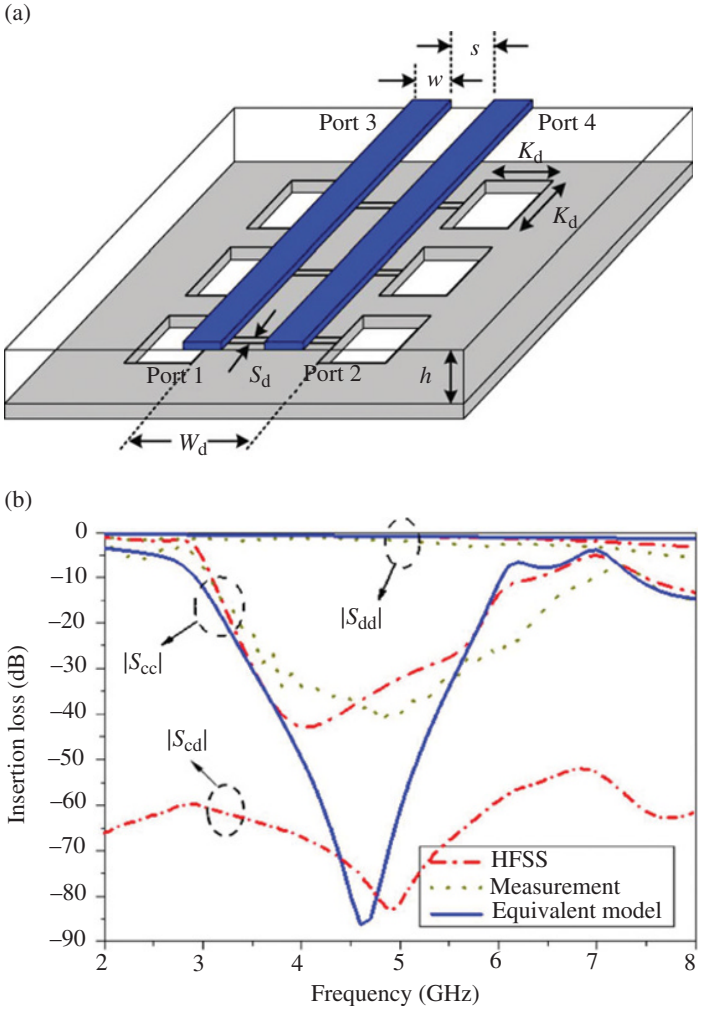


**FIGURE 6.10** Differential microstrip line with common-mode suppression based on slotted dumbbell-shaped resonators (a) and frequency response (b). Insertion loss for the differential and common mode are denoted by $S_{dd}$ and $S_{cc}$, respectively; mode conversion is determined by $S_{cd}$. Reprinted with permission from Ref. [16]; copyright 2008 IEEE.

separation. Figure 6.11a depicts a fabricated differential line loaded with symmetrically etched, square-shaped and tightly coupled CSRRs. The common-mode and differential-mode insertion loss are depicted in Figure 6.11b, and reveal that CSRRs are efficient elements to suppress the common-mode over a wide band, whilst the differential mode is transmitted in that band. A comparison between the CSRR-based approach and other approaches (excluding multilayered structures) indicates that the combination of size, design and fabrication simplicity, and common-mode rejection bandwidth in CSRR-loaded differential lines is very competitive [18].

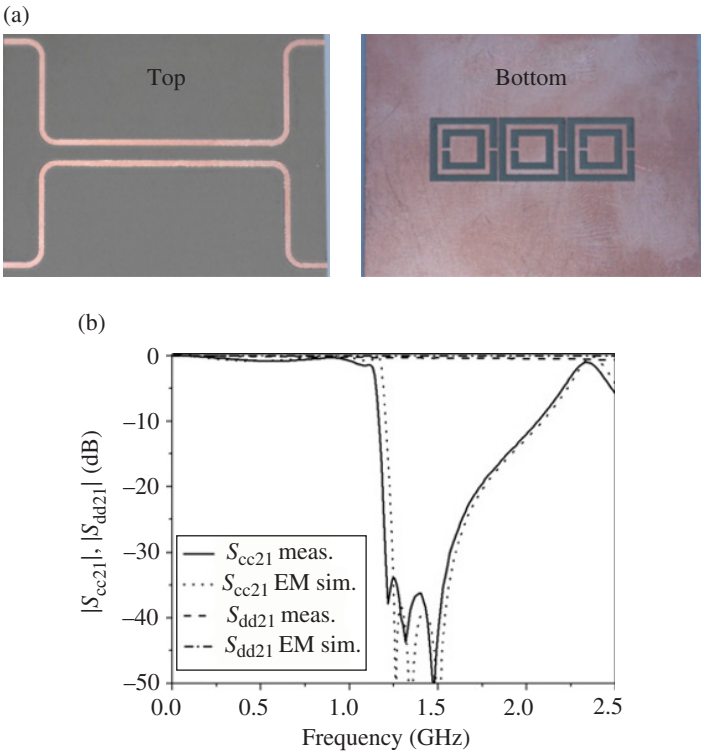


**FIGURE 6.11** Photograph (a) and common-mode ($|S_{cc21}|$) and differential-mode ($|S_{dd21}|$) insertion loss (b) of a differential line with wideband common-mode rejection based on CSRRs. Reprinted with permission from Ref. [18]; copyright 2011 IEEE.

### 6.3.2 CSRR- and DS-CSRR-Based Differential Lines with Common-Mode Suppression: Filter Synthesis and Design

As discussed earlier, common-mode filters based on CSRRs provide significant rejection bandwidths for that mode. Actually, bandwidth requirements are dictated by the differential signals. Namely, in order to prevent unwanted common-mode noise in differential lines, it is necessary that the suppressed band for the common mode extends at least beyond the limits of the required band for differential signal transmission. Therefore, rather than pursuing a specific rejection bandwidth, common-mode filters must be typically designed to satisfy a predefined common-mode rejection level within a certain frequency band.

To design CSRR-based common-mode filters following a systematic design approach, a circuit model that describes the CSRR-loaded differential line, including inter-resonator coupling, is necessary. In this regard, two limitations arise. First of all, the convenient CSRRs to achieve a wide common-mode stopband (with wide slots and interslot distance) cannot be considered to be electrically small, and hence they cannot be described by an accurate circuit model over a wide band. Second, the CSRRs must be oriented with their symmetry plane aligned with the symmetry plane

of the differential line. Under these conditions, mixed coupling (electric and magnetic) may arise, as discussed in Subsection 3.5.2.4, and the circuit model (provided the CSRRs are electrically small) is even more complex. This second aspect can be ignored to a first-order approximation, since a very accurate determination of the common-mode stop bandwidth is not required. Concerning the first aspect, if CSRRs are used as filtering elements, they must be electrically small in order to be accurately described by a lumped element equivalent circuit model. However, this is contrary to bandwidth enhancement. An intermediate solution is the use of DS-CSRRs (which is derived by application of duality to the DS-SRR introduced in Subsection 3.3.1.3—see Subsection 3.3.2.1), as pointed out in Ref. [19]. By driving the slot width and separation to the minimum value allowed by the available technology, DS-CSRRs can be considered to be electrically small, and the circuit model provides a reasonable description of the loaded differential lines. Such circuit model (unit cell), valid for electrically small CSRRs or DS-CSRRs, and neglecting magnetic coupling between the line and the resonators, is depicted in Figure 6.12a. In this model, the circuit parameters are identical to those of Figure 3.44b, except $L_m$ and $C_m$ that account for the magnetic and electric coupling, respectively, between the pair of lines.

The lumped-element equivalent circuit model for the even and odd modes are depicted in Figure 6.12b and c, respectively. For the differential mode, the resulting circuit model is simply the circuit model of an ordinary line with modified parameters. The circuit model for the even mode is formally identical to that of CSRR-loaded

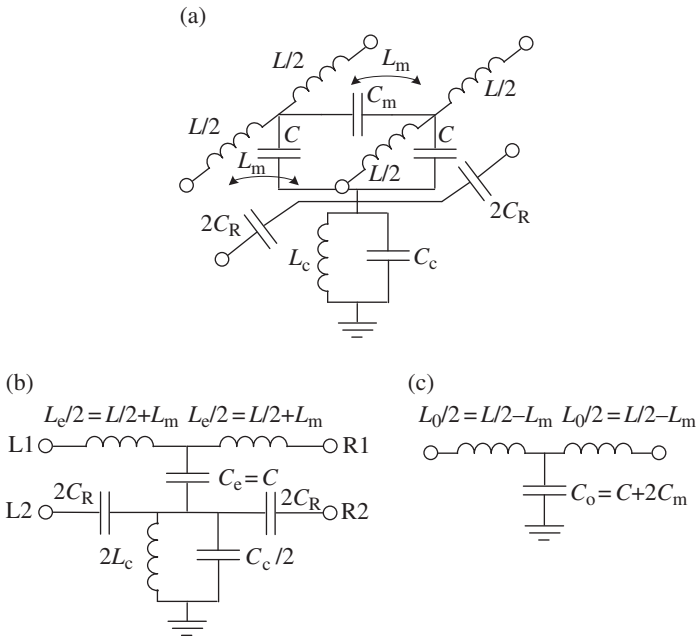


**FIGURE 6.12** Lumped-element equivalent circuit model (unit cell) of a differential microstrip line loaded with CSRRs or DS-CSRRs (a), equivalent circuit model for the even-mode (b), and equivalent circuit model for the odd-mode (c).

single-ended microstrip lines with inter-resonator coupling (Fig. 3.44b). Therefore, the analysis carried out in Subsection 3.5.2 to obtain the dispersion relation in CSRR-loaded single-ended lines is also valid to obtain the dispersion relation for the common mode in CSRR- or DS-CSRR-loaded differential lines. In particular, the common-mode rejection bandwidth for an infinite structure (in practice for a differential line with a large number of cells) can be estimated if the elements of the circuit model for the common mode are known.

For common-mode filter design and estimation of the common-mode rejection bandwidth, the procedure is as follows. For the reasons explained before, relative to the validity of the models of Figure 6.12 and fabrication tolerances, the slot width and separation are set to a minimum implementable value with the technology in use (for instance $c = d = 200$ μm [19]). Notice that this reduces the degrees of freedom and eases the common-mode filter design. Square-shaped resonators (rather than circular) are considered, in order to enhance the electric coupling between the differential line and the resonators and between adjacent resonators as well. To further enhance inter-resonator coupling, the separation between adjacent resonators is also set to that limiting value (200 μm). In order to achieve a strong electric coupling between the pair of lines and the resonator, the lines must be fitted inside the CSRR (or DS-CSRR) region and must be as wide as possible, and hence as uncoupled as possible (line dimensions can easily be inferred from a transmission line calculator). The side length of the resonator is determined from the model of the CSRR reported in Ref. [22] (which gives an estimation of $L_c$ and $C_c$) and the per-unit length capacitance of the coupled lines for the even mode (which gives $C_e$). The transmission zero frequency, given by

$$f_z = \frac{1}{2\pi\sqrt{2L_c(C_e + C_c/2)}} \tag{6.11}$$

is adjusted to the required filter central frequency, and this provides the CSRR side length (for a DS-CSRR the side length can also be determined by taking into account that the inductance is four times smaller than the inductance of the CSRR). Obviously, optimization of the resonator side length in order to fit the required central frequency is necessary.

With the previous procedure, the common-mode filter dimensions are perfectly determined. To predict the maximum achievable bandwidth, that is, the bandwidth obtained by considering an infinite number of cells, the dispersion relation given by (3.96) is used. However, since optimization at the layout level is required, it is necessary to extract the parameters of the circuit model following the procedure reported in Ref. [23] (and detailed in Appendix G). Thus, $L_e$, $C_e$, $L_c$, and $C_c$ are first extracted by considering a single-cell structure, and then $C_R$ is adjusted to fit the EM simulation of an order-2 common-mode filter. Once the circuit parameters are known, expression (3.96) can be evaluated, and the common-mode stopband can be estimated.

Following the previous approach, the maximum achievable rejection bandwidth for different CSRR and DS-CSRR common-mode filters was obtained. The rejection bandwidth was also obtained from full-wave EM simulations (the results are depicted in Fig. 6.13). The extracted circuit parameters and estimated fractional bandwidths are shown in Table 6.1.

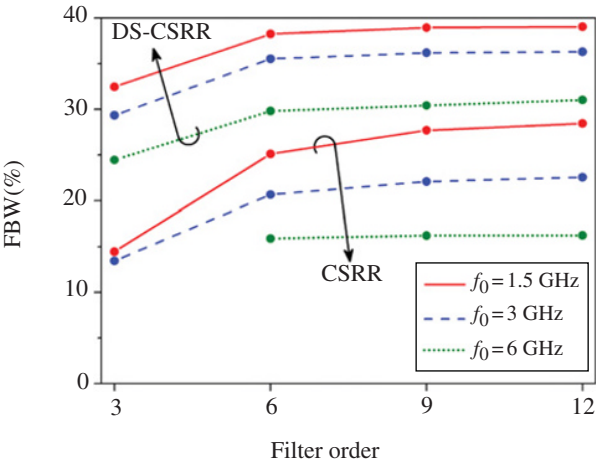


**FIGURE 6.13** Fractional rejection bandwidth (*FBW*) at −20 dB for the common mode given by EM simulation for CSRR- and DS-CSRR-loaded differential lines. Dimensions are for the CSRRs and DS-CSRRs, $c = d = 0.2$ mm, and *inter-resonator distance* = 0.2 mm; for the CSRRs, *side length* = 7.3 mm ($f_0 = 1.5$ GHz), 4.3 mm ($f_0 = 3$ GHz), and 2.6 mm ($f_0 = 6$ GHz); for the DS-CSRRs, *side length* = 13.8 mm ($f_0 = 1.5$ GHz), 7.5 mm ($f_0 = 3$ GHz), and 4.3 mm ($f_0 = 6$ GHz); for the differential line, $2W + S = side\ length - 2(2c - d) + 0.4$ mm, exhibiting a 50 Ω characteristic impedance (odd mode). The considered substrate is the *Rogers RO3010* with thickness $h = 1.27$ mm, and dielectric constant $\varepsilon_r = 10.2$. Reprinted with permission from Ref. [19]; copyright 2012 IEEE.

**TABLE 6.1 Extracted parameters and maximum fractional bandwidth inferred from the circuit model**

| $f_0$(GHz) | $L_e$(nH) | $C_e$(pF) | $L_c$(nH) | $C_c$(pF) | $C_R$(pF) | FBW(%) |
|---|---|---|---|---|---|---|
| CSRR-loaded differential lines | | | | | | |
| 1.5 | 6.3 | 1.1 | 2.1 | 3.2 | 0.05 | 30.7 |
| 3 | 4.2 | 0.5 | 1.0 | 2.0 | 0.03 | 26.4 |
| 6 | 3.0 | 0.2 | 0.4 | 1.4 | 0.04 | 20.7 |
| DS-CSRR-loaded differential lines | | | | | | |
| 1.5 | 15.9 | 1.6 | 1.0 | 8.6 | 0.32 | 32.6 |
| 3 | 9.0 | 0.8 | 0.45 | 4.8 | 0.09 | 29.4 |
| 6 | 6.9 | 0.3 | 0.15 | 3.6 | 0.05 | 23.6 |

By comparing the fractional bandwidths predicted by the reported approach with the saturation values of Figure 6.13, it can be concluded that the reported approach is more accurate for CSRR-loaded lines, as expected. Figure 6.14 compares the circuit and EM simulation (common mode) of the order 1, 2, and 3 CSRR-based common-mode filters designed to exhibit a central frequency of 1.5 GHz (in the circuit simulation the inter-resonator capacitance at input and output ports has been left opened since the CSRRs of the input and output cells are not externally fed, resulting in a two-port circuit). There is good agreement between the circuit and EM simulation,

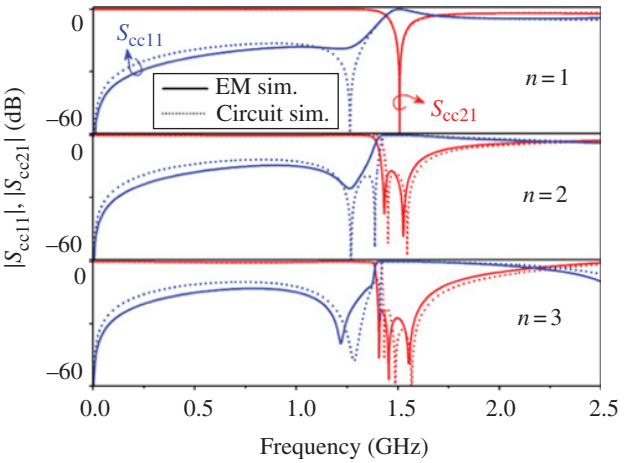


**FIGURE 6.14** Common-mode return loss $|S_{cc11}|$ and insertion loss $|S_{cc21}|$ given by the EM and circuit simulation for the order 1, 2, and 3 common-mode filters (1.5 GHz central frequency) based on CSRRs. Dimensions and substrate are indicated in the caption of Figure 6.13. Circuit parameters are given in Table 6.1. Reprinted with permission from Ref. [19]; copyright 2012 IEEE.

pointing out the accuracy of the model for CSRR-loaded lines with narrow slots, $c$, and interslot distance, $d$.

As can be seen in Figure 6.13, six resonators are enough to nearly achieve the maximum rejection bandwidth. Obviously, common-mode filter size can be reduced by decreasing the number of resonators but at the expense of a reduced common-mode rejection bandwidth. Thus, following a systematic approach based on the circuit model of the common mode, it can be inferred whether a specified rejection bandwidth and central frequency can be roughly fulfilled or not. If the required bandwidth is wider, we are forced to consider resonators with wider slots ($c$) and interslot distance ($d$), or, alternatively, multiple-tuned resonators. In these cases, however, filter design and maximum bandwidth estimation are not so straightforward.

### 6.3.3 Applications of CSRR and DS-CSRR-Based Differential Lines

In this subsection, it is demonstrated that the suppression of the even mode in differential lines loaded with DS-CSRRs does not affect the integrity of the differential signals. Subsequently, it is shown that by cascading a DS-CSRR to the input and output port of a balanced bandpass filter, common-mode suppression within the differential filter pass band can be substantially improved.

***6.3.3.1 Differential Line with Common-Mode Suppression*** In this subsection, the design procedure of a common-mode filter similar to that reported in Figure 6.11, but using DS-CSRRs, is reported. The target is to implement a common-mode filter

roughly centered at 1.35 GHz and exhibiting at least 35% fractional bandwidth (at 20 dB rejection level). According to the previous methodology, these specifications cannot be fulfilled by using CSRRs with $c = d = 200$ μm. However, it is possible to achieve these filter requirements by means of DS-CSRRs. Indeed, the estimated maximum bandwidth for a common-mode filter centered at 1.35 GHz was found to be 37.3% (considering the substrate of Fig. 6.13), but we do expect a larger value since the model tends to slightly underestimate the maximum achievable bandwidth for DS-CSRR-loaded lines (this can be appreciated by comparing Table 6.1 and Fig. 6.13). Moreover, for comparison purposes, a rectangular-shaped DS-CSRR was considered with its transverse side length identical to that of the CSRR reported in Figure 6.11. This favors the electric coupling between the pair of lines and the DS-CSRRs, and hence the common-mode stopband expansion (the reason is that the DS-CSRR longitudinal side is longer than the transverse one, and this increases the coupling capacitance $C_e$ as compared to that of a square-shaped DS-CSRR with identical transmission zero frequency). The longitudinal side length is thus the single-design parameter, and this has been determined following the same approach applied to square-shaped particles (the geometrical parameters of the structure are given in the caption of Fig. 6.15).

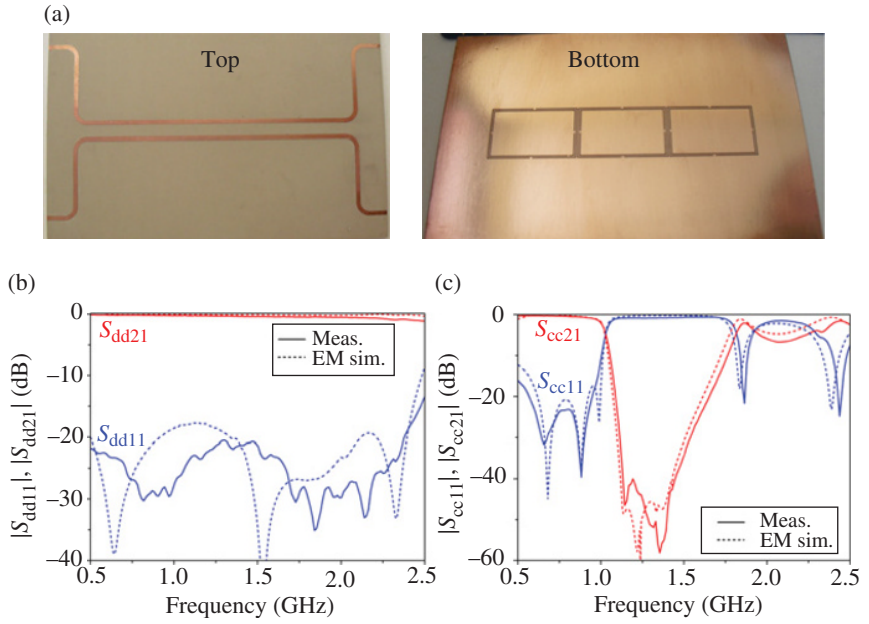


**FIGURE 6.15** Photograph (a), differential-mode return loss $|S_{dd11}|$ and insertion loss $|S_{dd21}|$ (b), and common-mode return loss $|S_{cc11}|$ and insertion loss $|S_{cc21}|$ (c) of the designed differential line with common-mode suppression based on DS-CSRRs. Dimensions are for the DS-CSRRs, $c = d = 0.2$ mm, *longitudinal side length* = 17.6 mm, and *transverse side length* = 10.8 mm; *inter-resonator distance* = 0.2 mm; for the differential line, $W = 1$ mm, and $S = 2.5$ mm. The considered substrate is the *Rogers RO3010* with thickness $h = 1.27$ mm, dielectric constant $\varepsilon_r = 10.2$, and loss tangent $\tan\delta = 0.0023$. Reprinted with permission from Ref. [19]; copyright 2012 IEEE.

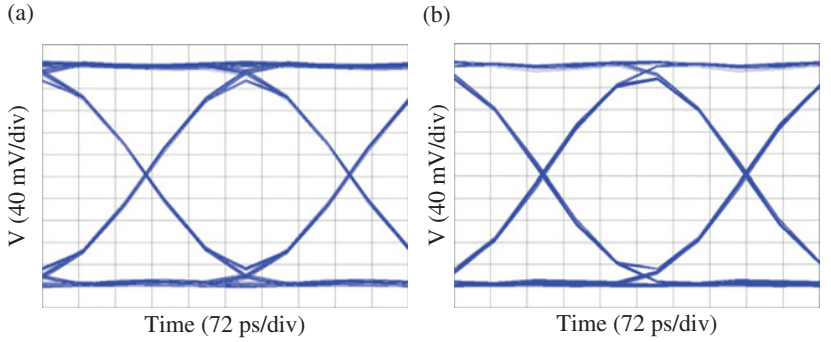


**FIGURE 6.16** Measured differential eye diagrams for the differential line of Figure 6.15 with (a) and without (b) DS-CSRRs. Reprinted with permission from Ref. [19]; copyright 2012 IEEE.

**TABLE 6.2 Measured eye parameters**

| | With DS-CSRRs | Without DS-CSRRs |
|---|---|---|
| Eye height | 278 mV | 281 mV |
| Eye width | 371 ps | 383 ps |
| Jitter (PP) | 29.3 ps | 16.9 ps |
| Eye-opening factor | 0.76 | 0.76 |

The photograph and frequency responses of the device, an order-3 common-mode filter, are depicted in Figures 6.15a–c (this filter order was found to be enough to satisfy the bandwidth requirements). As it can be seen, the differential signal is almost unaltered, whilst the common mode is rejected within a fractional bandwidth (41%) comparable to that achieved in Figure 6.11 by using CSRRs with wide and widely spaced rings. The DS-CSRR-based structure is a bit larger than that reported in Figure 6.11, but the design was done following the systematic procedure explained in the previous subsection.

Figure 6.16 shows the measured differential eye diagrams[5] with the excitation of 0.2 V amplitude in 2.5 Gb/s for the differential line of Figure 6.15a with and without DS-CSRRs. The eye diagram quality in terms of eye height, eye width, jitter, and eye-opening factor is compared for these two structures (see Table 6.2). According to these

[5] An eye diagram is an indicator of the quality of signals in high-speed digital transmissions. The eye diagram is constructed from a digital waveform by folding the parts of the waveform corresponding to each individual bit into a single graph with signal amplitude on the vertical axis and time on horizontal axis. By repeating this construction over many samples of the waveform, the resultant graph will represent the average statistics of the signal and will resemble an eye. The parameters indicated in Table 6.2 are defined in many sources focused on signal integrity. In brief, eye height is a measure of the vertical opening of an eye diagram, and it is determined by noise, which "closes" the eye. Eye width is a measure of the horizontal opening of an eye diagram, and it is calculated by measuring the difference between the statistical mean of the crossing points of the eye. Jitter is the time deviation from the ideal timing of a data-bit event. To compute jitter, the time deviations of the transitions of the rising and falling edges of an eye diagram at the crossing point are measured.

results, the presence of the DS-CSRRs does not significantly degrade the differential mode. The peak-to-peak jitter varies notably, but it is still within very acceptable limits for the DS-CSRR-based structure. Moreover, the eye-opening factor, which measures the ratio of eye height and eye amplitude, is identical in both structures.

#### *6.3.3.2 Differential Bandpass Filter with Enhanced Common-Mode Rejection*

Differential bandpass filters with common-mode rejection have been reported in the literature [24–36]. In this subsection, a balanced filter consisting of a pair of coupled folded stepped impedance resonators (SIRs) fed by a differential line is reported. The layout is depicted in Figure 6.17a (other balanced filters based on SIRs have been reported in Refs [31, 32, 35, 36]). The filter by itself rejects the common mode due to the symmetry of the structure, since the symmetry plane of the resonator exhibits an electric wall at the first SIR resonance. Therefore, such resonators cannot be excited by means of common-mode signals, and the even mode is reflected back to the source due to the presence of the slots between the pair of SIRs. However, the rejection level of the common mode in the region of interest is very limited since it depends on the distance between resonators and such inter-resonator distance is dictated by filter specifications. However, the common mode can be further rejected by introducing (cascading) DS-CSRRs.

The proposed differential filter, a second-order Chebyshev bandpass filter with a central frequency of 1.37 GHz, a fractional bandwidth of 10%, and 0.1 dB ripple was reported in Ref. [19]. The considered substrate is the *Rogers RO3010* with thickness $h$ = 1.27 mm, and dielectric constant $\varepsilon_r = 10.2$. With these specifications and substrate, the layout of the filter is that depicted in Figure 6.17a (the design of the filter, out of the scope of this book, was done following the procedure described in Ref. [37]).

The frequency response of the filter (differential mode, $S_{dd21}$ and $S_{dd11}$) is shown in Figure 6.17c. The common-mode insertion loss ($S_{cc21}$), also depicted in the figure, exhibits a rejection level of about 20 dB in the pass band region. In order to enhance the common-mode rejection, two identical DS-CSRRs, as shown in Figure 6.17b, were cascaded to the filter. Such DS-CSRRs were designed to generate a stopband for the common mode in the pass band region of the differential filter and are identical to those of Figure 6.15. The presence of the DS-CSRRs does not affect the filter response (odd mode). However, by merely introducing two DS-CSRRs, the common-mode rejection is roughly increased up to 50 dB in the region of interest (see Fig. 6.17c). These results point out that DS-CSRRs provide an efficient path to enhance the common-mode noise rejection in balanced filters.

### 6.3.4 Balanced Filters with Inherent Common-Mode Suppression

The common-mode suppressed balanced filter reported in the previous subsection exhibits inherent common-mode suppression, but the rejection level in the differential filter pass band is small; and for this reason, DS-CSRRs have been cascaded to the filter. In this subsection, balanced filters with a high common-mode rejection ratio (CMRR) without the need to cascade additional filter stages are reported. This high CMRR is achieved by introducing transmission zeros for the common mode in

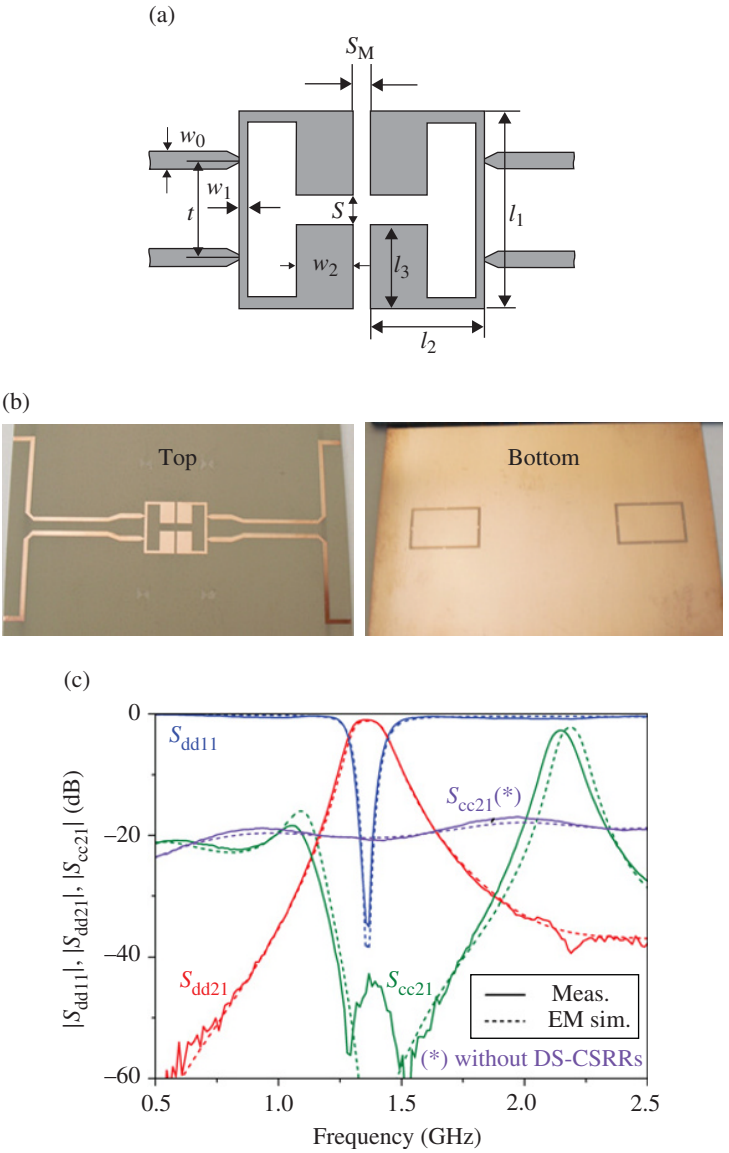


**FIGURE 6.17** Layout (a), photograph (b), and frequency response (c) of the designed differential bandpass filter with improved common-mode rejection. Dimensions are for the DS-CSRRs, $c = d = 0.2$ mm, *longitudinal side length* = 17.6 mm, and *transverse side length* = 10.8 mm; for the differential line, $W = 1$ mm, and $S = 2.5$ mm; for the differential filter, $S_M = 0.5$ mm, $s = 2$ mm, $w_0 = 1.2$ mm, $w_1 = 0.7$ mm, $w_2 = 3.7$ mm, $l_1 = 12.8$ mm, $l_2 = 7.5$ mm, $l_3 = 5.4$ mm, and $t = 5.5$ mm. The considered substrate is the *Rogers RO3010* with thickness $h = 1.27$ mm, dielectric constant $\varepsilon_r = 10.2$, and loss tangent $\tan\delta = 0.0023$. Reprinted with permission from Ref. [19]; copyright 2012 IEEE.

the differential filter pass band. By this means, the filter inherently and efficiently suppresses the common mode as will be shown in the two reported examples. The first one [34] combines OSRRs and OCSRRs, and can be considered the balanced version of the filters reported in Subsection Bandpass Filters Based on CRLH Lines Implemented by Means of OSRRs and OCSRRs. The second one [35] is based on mirrored SIRs to generate transmission zeros for the common mode.

***6.3.4.1 Balanced Bandpass Filters Based on OSRRs and OCSRRs*** Single-ended bandpass filters based on OSRRs and OCSRRs and consisting of a cascade of series-connected OSRRs alternating with shunt-connected OCSRRs were studied in Subsection 4.2.3.6. Since the OSRR and the OCSRR are described (to a first-order approximation) by means of a series and a parallel resonant tank, respectively, it follows that such structures synthesize the canonical circuit model of a bandpass filter. As it is discussed in [38], in microstrip technology, it is necessary to include metallic vias in the design in order to effectively ground the OCSRRs, and the ground plane is windowed in the regions beneath the OSRRs in order to obtain a more accurate description of the particle by means of a series resonator.

A typical layout (order 3) of the proposed OSRR/OCSRR-based differential bandpass filters is depicted in Figure 6.18. Notice that this structure is indeed the unit cell ($\pi$-model) of a balanced CRLH line. The structure is symmetric with respect to the indicated plane (dashed line). For the differential mode, where there is a virtual ground in that plane (electric wall), the OCSRRs are grounded (without the presence of vias), and the structure exhibits a pass band. If the distance between the host lines is large, no coupling effects take place between mirror elements and filter design is as simple as designing a single-ended bandpass filter.

The proposed strategy to suppress the common mode in the region of interest (i.e., the differential filter pass band) consists of tailoring the metallic region surrounding the OCSRRs. The lumped element equivalent circuit model of the four-port section corresponding to one pair of mirrored OCSRRs is depicted in Figure 6.19a [34].

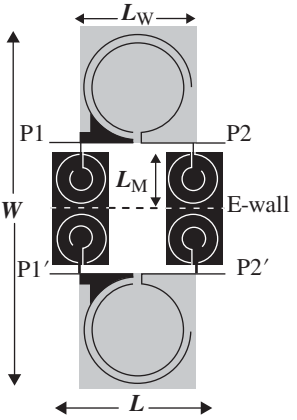


**FIGURE 6.18** Typical layout of the proposed OSRR/OCSRR-based differential-mode bandpass filter ($\pi$-network, order-3) with common-mode suppression.

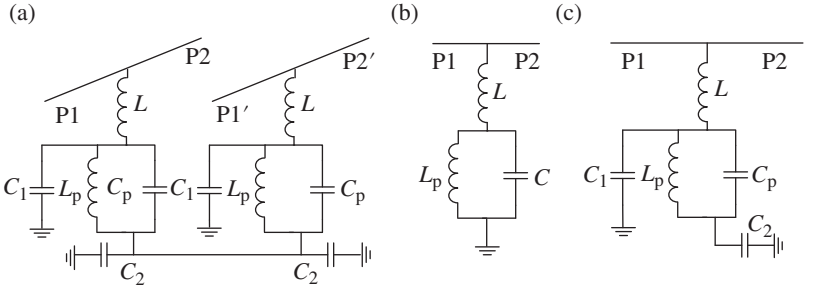


**FIGURE 6.19** Equivalent circuit model of the mirrored OCSRR pair section. (a) complete model, (b) differential-mode model, and (c) common-mode model.

$L_p$ and $C_p$ model the OCSRR, $L$ accounts for the inductive strip present between the microstrip lines and the center part of the OCSRRs, $C_1$ is the capacitance between the central metallic region of the OCSRR and the ground plane; finally, $C_2$ is the patch capacitance corresponding to the metallic region surrounding the OCSRRs. The models for the differential and common-modes are depicted in Figures 6.19b and c, respectively. Notice that the capacitance $C_2$ is grounded for the differential-mode and does not play any role for that mode. Thus, for this mode, the shunt OCSRR is described by a parallel resonator in series with an inductor (this inductor is useful to introduce a transmission zero above the differential filter pass band). However, for the common mode, the symmetry plane is an open circuit, and the effect of the capacitance $C_2$ is the presence of two transmission zeroes in the common-mode frequency response. Once the elements $L$, $L_p$, $C_p$, and $C_1$ are set to satisfy the differential-mode filter response (including the transmission zero above the pass band), $C_2$ must be adjusted to set the first transmission zero of the common-mode frequency response in the centre of the differential-mode pass band.

The reported example is a balanced filter with the following specifications [34]: order $n = 3$, Chebyshev response with fractional bandwidth FBW = 45%, central frequency $f_o = 1$ GHz, and 0.05 dB ripple. From these specifications, the elements of the canonical π-network order-3 bandpass filter can be obtained through well-known transformations from the lowpass filter prototype. Once these elements are known, the topology of the series-connected OSRRs is obtained by curve fitting the response of the series $LC$ resonator giving the ideal Chebyshev response in the region of interest. For the OCSRRs, the elements of the model of Figure 6.19b ($L$, $L_p$, and $C = C_1 + C_p$) are derived from the susceptance slope at $f_o$ (i.e., by forcing it to be equal to that of the $LC$ tank giving the ideal Chebyshev response), and from the differential-mode transmission zero, given by

$$f_Z^{dd} = \frac{1}{2\pi}\sqrt{\frac{1}{C}\left(\frac{1}{L}+\frac{1}{L_p}\right)} \tag{6.12}$$

The parasitic capacitances of the π-model of the OSRR (which can be easily extracted from the EM simulation of the isolated particle) are small and have negligible effect on the differential filter response. Once $L$, $L_p$, and $C$ are known, the OCSRRs are

synthesized with the help of the model reported in Ref. [39] (analyzed in Subsections 3.3.2.2 and 3.5.2.5) and the parameter extraction procedure reported in Appendix G. From this model, the OCSRR capacitance, $C_p$, can be estimated and hence $C_1$ can be derived. Finally, $C_2$ is adjusted to the required value to force the common-mode transmission zero at $f_o$. The metallic region surrounding the OCSRRs is then expanded or contracted to adjust the common-mode transmission zero to that value (the initial size is inferred from the parallel plate capacitor formula). Following this procedure, the element values and the layout of the shunt branch were inferred.

The photograph of the designed and fabricated filter is shown in Figure 6.20a (dimensions are $0.15\lambda_g \times 0.30\lambda_g$, $\lambda_g$ being the guided wavelength at the filter central frequency). Figure 6.20b shows the simulated and measured insertion and return loss for the differential mode, as well as the insertion loss for the common mode. The circuit simulations for the differential- and common-mode models are also included in the figure. Both the differential- and common-mode filter responses are in good agreement with the circuit simulations up to roughly 2 GHz. The agreement with the Chebyshev response is also good, although the selectivity and stop-band rejection above the pass band of the designed balanced filter are better due to the effects of the transmission zero (the first spurious appears at roughly $3f_o$). As expected, there is a transmission zero at $f_o$ for the common mode (the CMRR at $f_o$ being 53 dB), and the common-mode rejection within the differential filter pass band is better than 20 dB. The combination of filter size and common-mode rejection is very competitive, and this type of filters is especially suitable for wideband applications in differential systems.

***6.3.4.2 Balanced Bandpass Filters Based on Mirrored SIRs*** An alternative approach to implement differential-mode bandpass filters with inherent common-mode suppression consists on using mirrored SIRs coupled through admittance inverters. The typical topology (order-3) for these filters is depicted in Figure 6.21, where the impedance inverters are implemented by means of 90° meandered lines for size reduction. The equivalent circuit model of the structure is depicted in Figure 6.22a, where $J_{i,i+1}$ denotes the admittance of the inverters, $C_{pi}$ are the patch capacitances of the square transmission line sections cascaded to the inverters, $L_{pi}$ are the inductances of the narrow strips of the mirrored SIRs, and finally, $C_{zi}$ are the capacitances of the central patches. The circuit models for the differential and common modes are depicted in Figures 6.22b and c. For the differential mode, the symmetry plane is an electric wall, and the capacitances $C_{zi}$ are grounded. The resulting structure is thus the canonical circuit of a bandpass filter, consisting of a cascade of parallel LC resonators coupled through admittance inverters. For the common mode, the symmetry plane is a magnetic wall, and the equivalent circuit exhibits a stopband behavior. Indeed, except for the presence of the capacitances $C_{pi}$, such circuit is the canonical circuit of a stopband filter. As long as the inverters exhibit their functionality in a narrow (or moderate) band, the synthesis of balanced filters with standard responses (Chebyshev or Butterworth) following this approach is bandwidth limited. Nevertheless, it is possible to generate balanced filters with significant bandwidths, as reported in the next example.

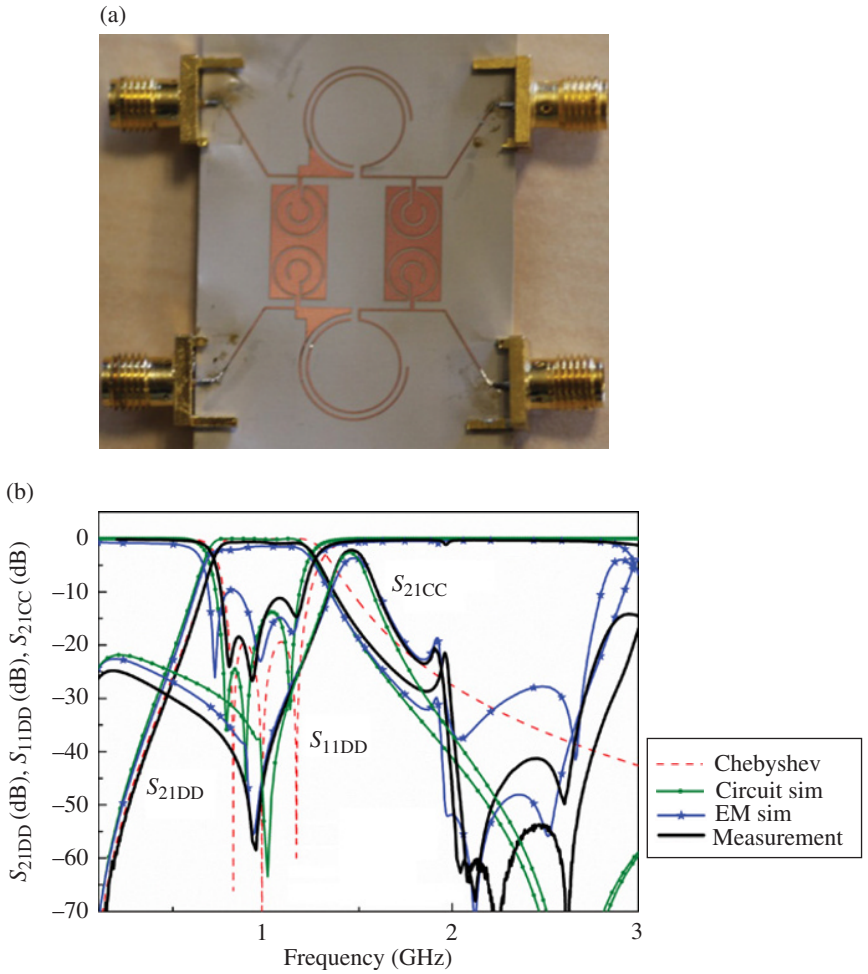


**FIGURE 6.20** Photograph (a) and frequency response (b) of the fabricated balanced OSRR/OCSRR-based bandpass filter. The considered substrate is the *Rogers RO3010* with dielectric constant $\varepsilon_r = 10.2$ and thickness $h = 0.254$ mm. Dimensions (in reference to Fig. 6.18) are $L = 18.9$ mm, $W = 37.8$ mm, $L_W = 12.6$ mm, and $L_M = 6$ mm. For the OCSRR, $r_{ext} = 2.7$ mm, $c = 0.2$ mm, and $d = 1.2$ mm. For the OSRR, $r_{ext} = 5.8$ mm, $c = 0.2$ mm, and $d = 0.55$ mm. The 50 Ω microstrip lines have a width of 0.21 mm. For the π-model of the OSRR (Fig. 3.56e), the elements of the series LC tank are 22.28 nH and 1.22 pF, the values of the shunt capacitors are 1.35 pF (left) and 0.74 pF (right) and $L_{m1}$ and $L_{m2}$ have negligible values. The elements of the shunt branch are $L = 0.628$ nH, $L_p = 3.675$ nH, $C_p = 0.1$ pF, $C_1 = 6.85$ pF, and $C_2 = 5.65$ pF. Reprinted with permission from Ref. [34]; copyright 2013 IEEE.

Let us consider the implementation of an order-3 balanced common-mode suppressed Chebyshev bandpass filter with central frequency $f_o = 2.4$ GHz, 0.15 dB ripple, and fractional bandwidth FBW = 40% [35]. Identical LC parallel resonators (those of the differential-mode circuit, $L_p$ and $C_p$) and admittance inverters with

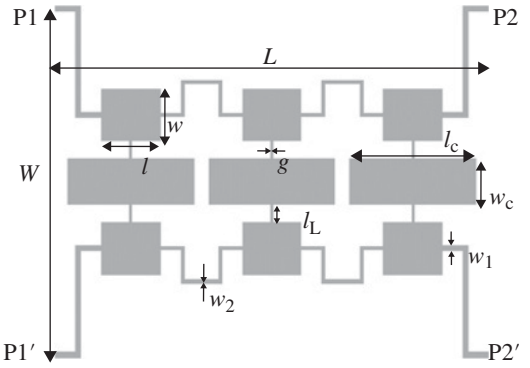


**FIGURE 6.21** Typical layout (order-3) of a differential-mode bandpass filter with common-mode suppression based on mirrored SIRs and admittance inverters.

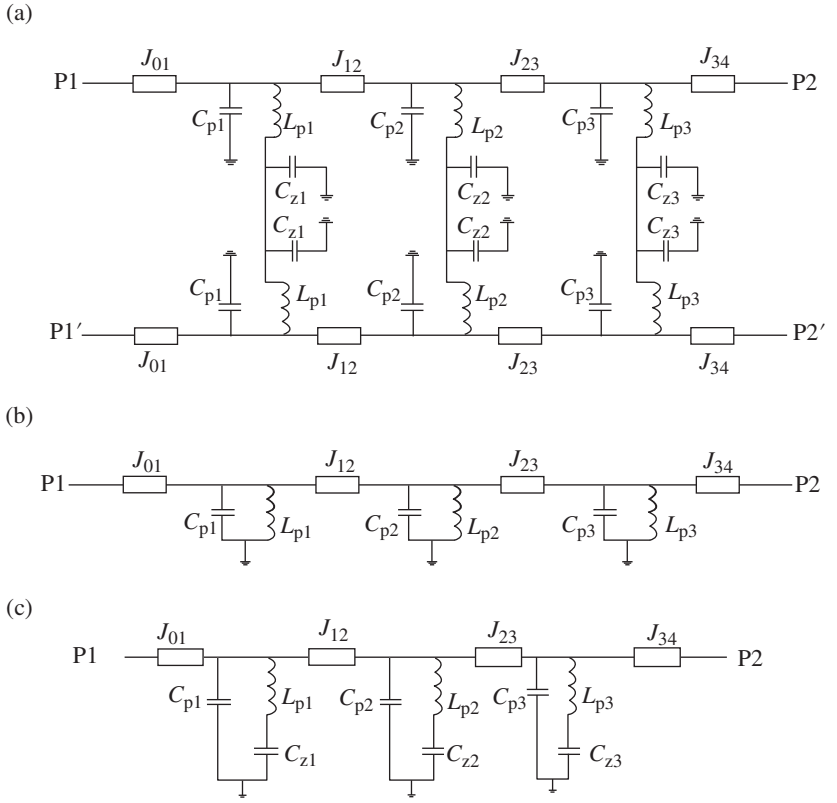


**FIGURE 6.22** Circuit model of the balanced bandpass filter of Figure 6.21 (a), and equivalent circuits for the differential (b) and common (c) modes.

variable admittance have been considered. By applying the well-known transformations from the lowpass filter prototype [37], the element values are found to be $L_p$ = 1.465 nH and $C_p$ = 3 pF, and the admittances of the inverters are $J_{01} = J_{34} = 0.0178$S and $J_{12} = J_{23} = 0.0157$ S. For the suppression of the common mode, the transmission zeros, given by the resonances of the series resonators $L_{pi} - C_{zi}$, were forced to be identical and equal to the central frequency of the differential-mode response, $f_o$. Since the inductances $L_p$ are determined by the differential-mode filter specifications, it follows that $C_z = 2.925$ pF.

To implement this filter, the widths of the transmission line sections corresponding to the calculated admittances of the inverters were obtained by means of a transmission line calculator (the considered substrate is the *Rogers RO3010*, with thickness $h = 0.635$ mm and dielectric constant $\varepsilon_r = 10.2$). Patch dimensions of the capacitances $C_p$ were calculated from the well-known formula giving the capacitance of an electrically short low-impedance transmission line section (see Chapter 1). Finally, the dimensions of the pair of grounded resonators $L_p - C_z$ implemented through mirrored SIRs were calculated in order to accurately synthesize the required elements values up to at least $2f_o$, according to the procedure reported in Ref. [40]. The photograph of the fabricated device is shown in Figure 6.23a. Total filter size is 26.49 mm × 32.78 mm, that is, $0.51\lambda_g \times 0.63\lambda_g$, $\lambda_g$ being the guided wavelength at $f_o$. The simulated (using the *Agilent Momentum* commercial software) and measured frequency responses of the filter for the differential- and common-mode are depicted in Figure 6.23b, together with the circuit simulations and the ideal Chebyshev response. The agreement between circuit simulation, EM simulation, and measurement is very good, and validates the circuit model and the proposed methodology for common-mode suppressed balanced filter design. The measured differential insertion loss is better than 0.5 dB, the maximum differential return losses are 28 dB in the pass band, and the differential stopband exhibits a rejection better than 12 dB up to $2f_o$. The measured common-mode rejection within the differential filter pass band is better than 45 dB and the CMRR at $f_o$ is better than 60 dB. Although the filter of Figure 6.23 is electrically larger than the one of Figure 6.20, one key advantage of balanced filters based on the topology of Figure 6.21 is the absence of defects in the ground plane.

It is worth mentioning that by replacing the impedance inverters in the structure of Figure 6.21 with series resonant elements (e.g., implemented by inductive strips and interdigital capacitors), a compact balanced CRLH line with intrinsic common-mode suppression results.[6] Such balanced artificial lines have been applied to the design of dual-band balanced power splitters [41] and ultra wideband (UWB) bandpass filters [42].

[6] Indeed, the structure of Figure 6.21 cannot be considered to be an artificial transmission line. However, it is included here since by merely replacing the inverters with LC series resonators, a differential CRLH structure results.

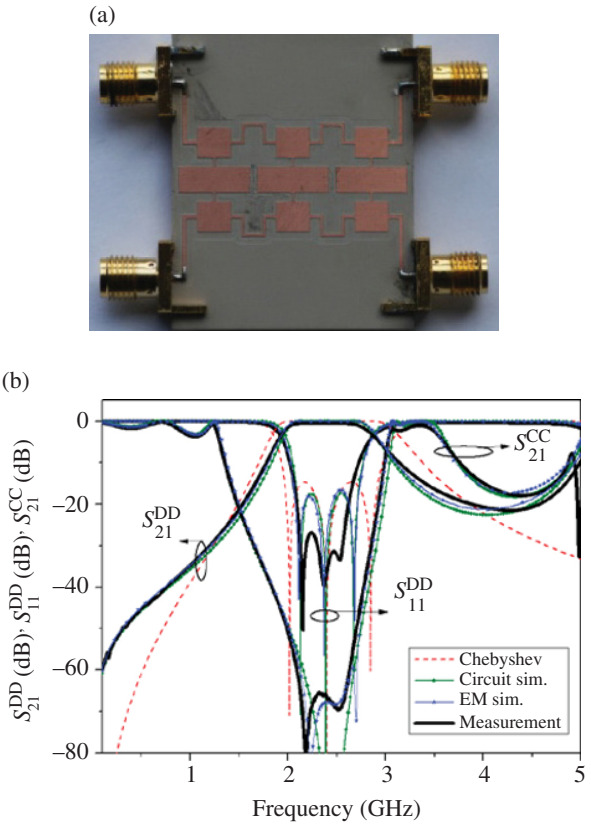


**FIGURE 6.23** Photograph (a) and frequency response (b) of the designed order-3 balanced bandpass filter. Dimensions (in reference to Fig. 6.21) are $W = 26.49$ mm, $L = 32.78$ mm, $w = 4$ mm, $l = 4.475$ mm, $g = 0.2$ mm, $l_L = 1.32$ mm, $l_C = 9.6$ mm, $w_C = 3.4$ mm, $w_1 = 0.434$ mm, and $w_2 = 0.297$ mm. Reprinted with permission from Ref. [35]; copyright 2013 IEEE.

## 6.4 WIDEBAND ARTIFICIAL TRANSMISSION LINES

The CRLH and the generalized CRLH transmission lines studied in Chapter 3 support wave propagation in a limited frequency band. In this section, two strategies to widen the propagation band in artificial transmission lines are reviewed. The first one is based on the lattice network and other related unit cell topologies. The second one uses active elements in order to implement non-Foster reactances.

### 6.4.1 Lattice Network Transmission Lines

In this subsection, the dispersion and characteristic impedance of the generalized lattice network are derived. It is shown that all-pass CRLH transmission lines with arbitrary order can potentially be synthesized with these structures [43]. However,

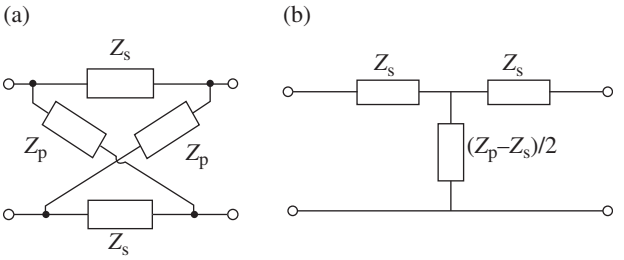


**FIGURE 6.24** Lattice-network unit cell (a) and its equivalent T-circuit model (b).

the implementation of such artificial lines is not so straightforward. Practical implementation limitations are discussed, and some prototypes of lattice network CRLH lines are presented in this section. Finally, other networks related to the lattice network, such as the bridged-T network, are introduced as a more practical approach for the implementation of broadband CRLH transmission lines.

***6.4.1.1 Lattice Network Analysis*** The artificial transmission lines considered in Chapter 3 are described either by a cascade of T or π unit cells. Let us now consider an X-type unit cell like the one shown in Figure 6.24a, that is, a lattice network [44],[7] with impedance $Z_s$ in the series branches and $Z_p$ in the cross diagonal arms. By calculating the elements of the impedance matrix, this two-port network can be transformed to its equivalent T-circuit model, depicted in Figure 6.24b. Using (2.33) and (2.30), the phase constant and characteristic (or iterative) impedance of the generalized lattice network of Figure 6.24a are given by[8]

$$\cos(\beta l) = \frac{Z_p + Z_s}{Z_p - Z_s} \tag{6.13}$$

$$Z_B = \sqrt{Z_s Z_p} \tag{6.14}$$

Let us now consider that the element of the series and cross branch is an inductor ($Z_s = j\omega L_R$) and a capacitor ($Z_p = -j/\omega C_R$), respectively (Fig. 6.25a). Evaluation of (6.13) and (6.14) gives

$$\cos(\beta l) = \frac{1 - L_R C_R \omega^2}{1 + L_R C_R \omega^2} \tag{6.15}$$

$$Z_B = \sqrt{\frac{L}{C}} \tag{6.16}$$

[7] Lattice networks have been used as phase equalizers, where the relative phase between the input and the output port varies with frequency, whereas the attenuation is constant at all frequencies. These structures have been also designated as all-pass lattice filters, and were already pointed out in 1923 by O. J. Zobel [44].
[8] Notice that (6.13) and (6.14) have been derived by identifying $(Z_p - Z_s)/2$, that is, the shunt impedance of the equivalent T-circuit model of the generalized lattice network, with $Z_p$ in expressions (2.30) and (2.33).

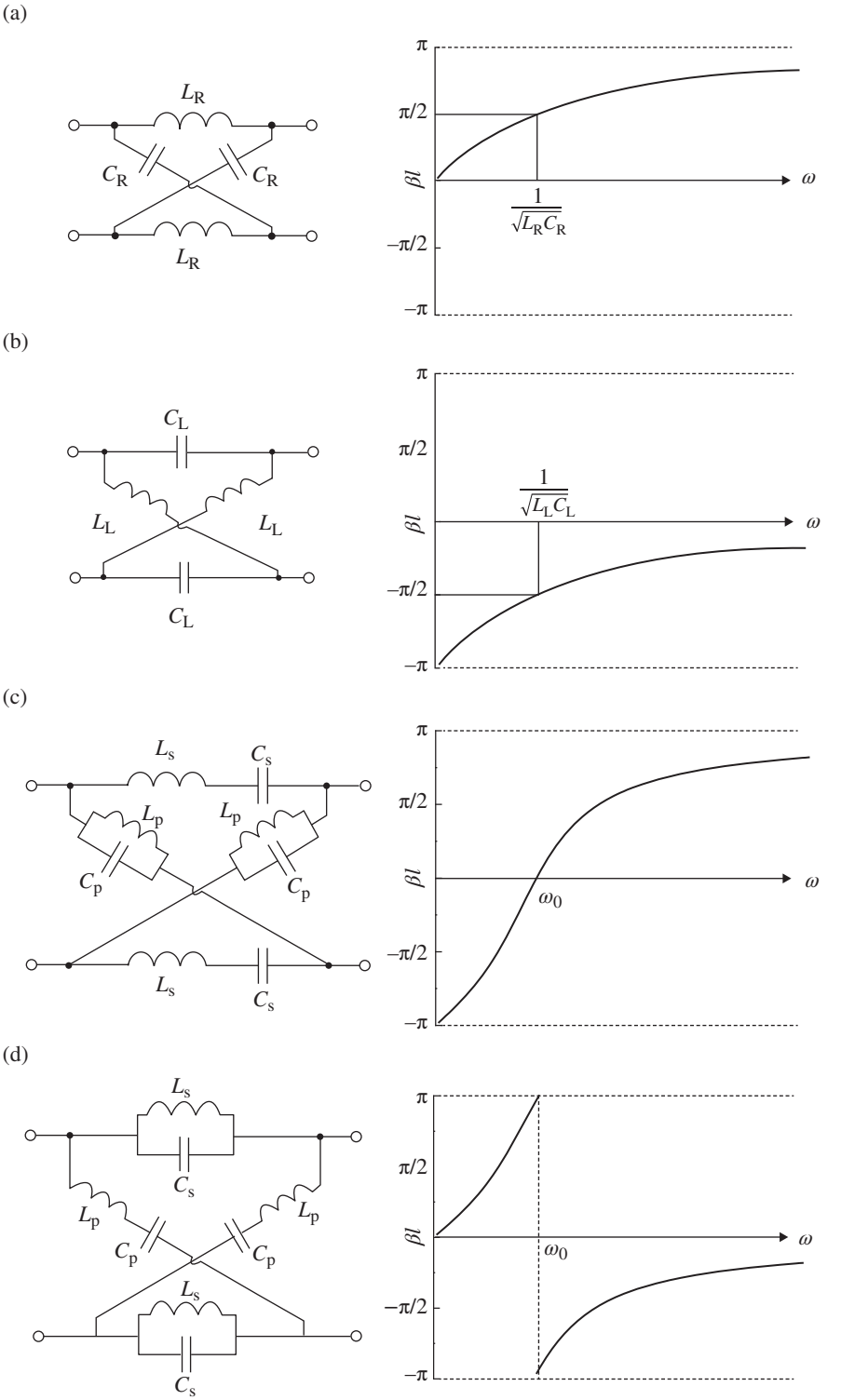


**FIGURE 6.25** Examples of lattice networks and their corresponding dispersion curves. (a) order-1 RH, (b) order-1 LH, (c) order-2 CRLH, and (d) order-2 D-CRLH.

with $L = L_R$ and $C = C_R$ in (6.16). Inspection of (6.15) and (6.16) reveals that the network of Figure 6.25a is an all-pass structure (the characteristic impedance is real and frequency independent, like the one of an ordinary transmission line), and that wave propagation is forward from DC up to unlimited frequencies (the dispersion diagram is also depicted in Fig. 6.25a). If the inductor and capacitor are interchanged (Fig. 6.25b), the characteristic impedance is also constant and given by (6.16), with $L = L_L$ and $C = C_L$, whereas the phase constant is found to be

$$\cos(\beta l) = -\frac{1 - L_L C_L \omega^2}{1 + L_L C_L \omega^2} \tag{6.17}$$

and wave propagation is backward in the whole EM spectrum (see the dispersion diagram depicted in Fig. 6.25b). If the phase shift is small enough, the networks of Figure 6.25a and b mimic a conventional line and a purely left-handed (PLH) line, respectively.

By adequately choosing the reactive elements of the series and cross arms of the X-network, all-pass CRLH structures of arbitrary order can be obtained [43]. For instance, Figure 6.25c and d show the lattice networks corresponding to order-2 all-pass CRLH and dual-CRLH lines, respectively. To obtain all-pass structures, it is necessary that the zeros and poles of the reactance of the series branch coincide with the zeros and poles of the susceptance of the cross branch (see Appendix I). For the specific case of order-2 lattice networks, the condition is similar to the balance condition for T- or π-type CRLH transmission lines:

$$\omega_s \equiv \frac{1}{\sqrt{L_s C_s}} = \frac{1}{\sqrt{L_p C_p}} \equiv \omega_p = \omega_o \tag{6.18}$$

where $L_s$ $C_s$ and $L_p$ $C_p$ are the reactive elements of the series branch and cross branch, respectively, and $\omega_o$ is the transition frequency. For the network of Figure 6.25c, expression (6.13), subjected to (6.18), rewrites as follows:

$$\cos(\beta l) = \frac{1 - L_s C_p \omega^2 \left(1 - \dfrac{\omega_o^2}{\omega^2}\right)^2}{1 + L_s C_p \omega^2 \left(1 - \dfrac{\omega_o^2}{\omega^2}\right)^2} \tag{6.19}$$

whereas the dispersion relation for the network of Figure 6.25d is

$$\cos(\beta l) = -\frac{1 - L_p C_s \omega^2 \left(1 - \dfrac{\omega_o^2}{\omega^2}\right)^2}{1 + L_p C_s \omega^2 \left(1 - \dfrac{\omega_o^2}{\omega^2}\right)^2} \tag{6.20}$$

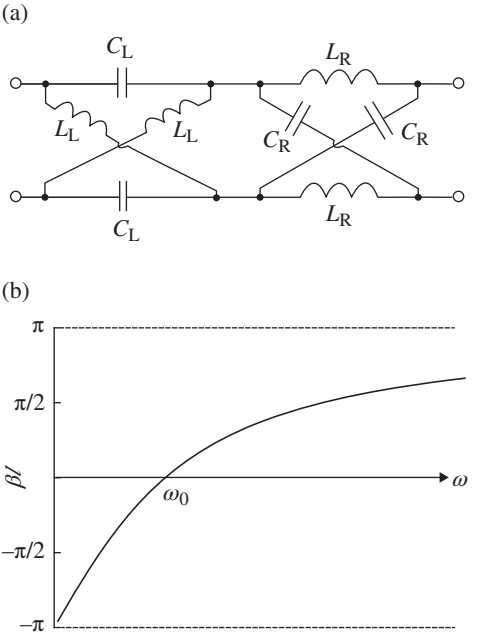


**FIGURE 6.26** CRLH artificial transmission line unit cell consisting of two cascaded order-1 X-type RH and LH cells (a), and dispersion diagram (b). Elements are $C_L = C_R = 1.061$ pF and $L_L = L_R = 2.652$ nH (i.e., $f_o = \omega_0/2\pi = 3$ GHz).

The dispersion curves are also depicted in Figure 6.25c and d. In both cases, the characteristic impedance is given by (6.16), with $L = L_s$ and $C = C_p$.

From a practical viewpoint, the physical implementation of the order-2 lattice networks of Figure 6.25c and d is not straightforward. An alternative to implement all-pass order-2 CRLH lines is to combine PLH and PRH X-type cells, as depicted in Figure 6.26a. In this case, the following condition must be satisfied:

$$\sqrt{\frac{L_R}{C_R}} = \sqrt{\frac{L_L}{C_L}} \equiv Z_B \tag{6.21}$$

which gives the characteristic impedance of the whole all-pass network. The transition frequency is given by that frequency satisfying:

$$\left|\arccos\left(\frac{1-L_R C_R \omega_o^2}{1+L_R C_R \omega_o^2}\right)\right| - \left|\arccos\left(-\frac{1-L_L C_L \omega_o^2}{1+L_L C_L \omega_o^2}\right)\right| = 0 \tag{6.22}$$

namely:

$$\omega_o = \frac{1}{\sqrt{L_R C_L}} = \frac{1}{\sqrt{L_L C_R}} \tag{6.23}$$

In particular, if $L_R C_R = L_L C_L$ (which, according to 6.21, means that $L_R = L_L$ and $C_R = C_L$), the transition frequency can also be expressed as follows:

$$\omega_o = \frac{1}{\sqrt{L_R C_R}} = \frac{1}{\sqrt{L_L C_L}} \tag{6.24}$$

corresponding to the frequency where the PLH cell and the PRH cell experience a phase shift of $\beta l = -90^\circ$ and $\beta l = +90^\circ$, respectively (thus providing an overall phase shift of $\beta l = 0^\circ$). Figure 6.26b shows the dispersion diagram corresponding to the structure of Figure 6.26a for the indicated element values.

It is worth mentioning that, despite that the networks of Figures 6.25c and 6.26a exhibit similar dispersion curves, there is not an element transformation that makes them equivalent. Notice that the dispersion relation (with the frequency variable in the $x$-axis) for the structure of Figure 6.26a is a concave function at all frequencies. However, for the order-2 CRLH X-type cell of Figure 6.25c, the dispersion relation is convex for frequencies below $\omega_o$, and concave above that frequency (i.e., there is an inflexion point at $\omega_o$). Although the synthesis of a cascaded order-1 LH and RH X-type cells is simpler than an order-2 CRLH lattice network, the former structure may present certain limitations due to the curvature of its dispersion relation. For instance, it is not possible to implement dual-band components based on dual-band ($\pm 90^\circ$) impedance inverters implemented with single-unit cells (like the one depicted in Fig. 6.26a) with a ratio of operating frequencies smaller than 3.

The synthesis of all-pass CRLH artificial lines can be further simplified by cascading an X-type LH unit cell with a transmission line section with identical characteristic impedance, as depicted in Figure 6.27a, or with a pair of transmission lines sections (at the input and output ports of the LH X-type cell). A typical dispersion curve for the structure of Figure 6.27a is depicted in Figure 6.27b. In this case, due to the presence of a distributed element, the phase of the structure grows indefinitely.[9]

***6.4.1.2 Synthesis of Lattice Network Artificial Transmission Lines*** X-type networks are balanced[10] structures with cross branches. Therefore, as mentioned earlier, their synthesis is not simple. CRLH artificial lines were implemented by Bongard *et al*. [45–47] by combining LH X-type cells and transmission line sections (the schematic is depicted in Fig. 6.28a). The structure reported in Ref. [47] utilizes paired strips technology (see Fig. 1.2) with two additional metal levels to implement the series capacitances of the LH X-type cells, and via holes to implement the cross inductances. The structure is shown in Figure 6.28b, and the S-parameters and phase of $S_{21}$ are depicted in Figure 6.28c and d, respectively, in the range 2 GHz–9 GHz.

[9] Although the dispersion curves of the structures depicted in Figures 6.25 and 6.26 are limited to $\pm\pi$, in practical structures the presence of a parasitic transmission line (and other parasitic effects) cannot be avoided. Therefore, deviations of the dispersion diagram (with regard to the theoretical one) at high frequencies are expected.

[10] Notice that the term "balanced" is used here as synonymous of "differential." Do not confuse with the term "balanced" applied to CRLH lines with continuous transition between the LH and the RH band.

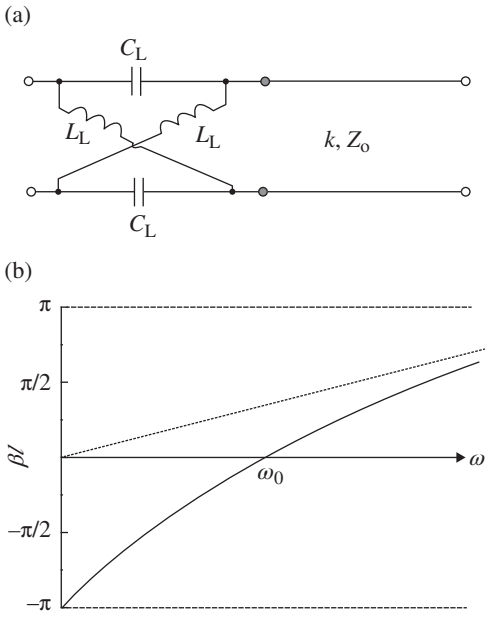


**FIGURE 6.27** CRLH artificial transmission line unit cell consisting of an order-1 X-type LH cell cascaded to an ordinary transmission line section with phase constant $k$ and characteristic impedance $Z_o$ (a), and dispersion diagram (b).

The structure was designed to exhibit a transition frequency at $f_o = 6$ GHz, and it can be appreciated from Figure 6.28 that it can be considered all-pass, at least in a very wide region in the vicinity of $f_o$.

Using the unit cell structure of Figure 6.28a, a broad-band (matched from DC to millimeter waves) silicon-integrated CRLH transmission line using a monolayer CPW host line was proposed [48] (see Fig. 6.29). The measurements carried out in Ref. [48] demonstrate a balanced CRLH behavior from 5 GHz up to 35 GHz, with a transition frequency at $f_o = 20$ GHz. The interesting aspect of the structure of Figure 6.29 is that it is implemented using a single-metal layer. Since the series capacitances must be implemented in both conductors of the transmission line, the ground conductors of the host CPW must be of finite width. The required capacitances were realized by interdigital capacitors; whereas for the implementation of the crossed inductors, the solution proposed in Ref. [48] was to implement each of the inductances in a different slot of the CPW. Since the resulting structure is strongly asymmetrical, the excitation of the odd parasitic mode was prevented by the use of the bridges shown in dark gray in Figure 6.29. Thus, the structure indeed uses two metal levels. Other X-type LH, RH, and CRLH planar structures implemented by using two metal levels are reported in Ref. [49].

At this point, it is worth mentioning that from the equivalence between terminated coupled line sections and lattice networks [50], another approach for the physical

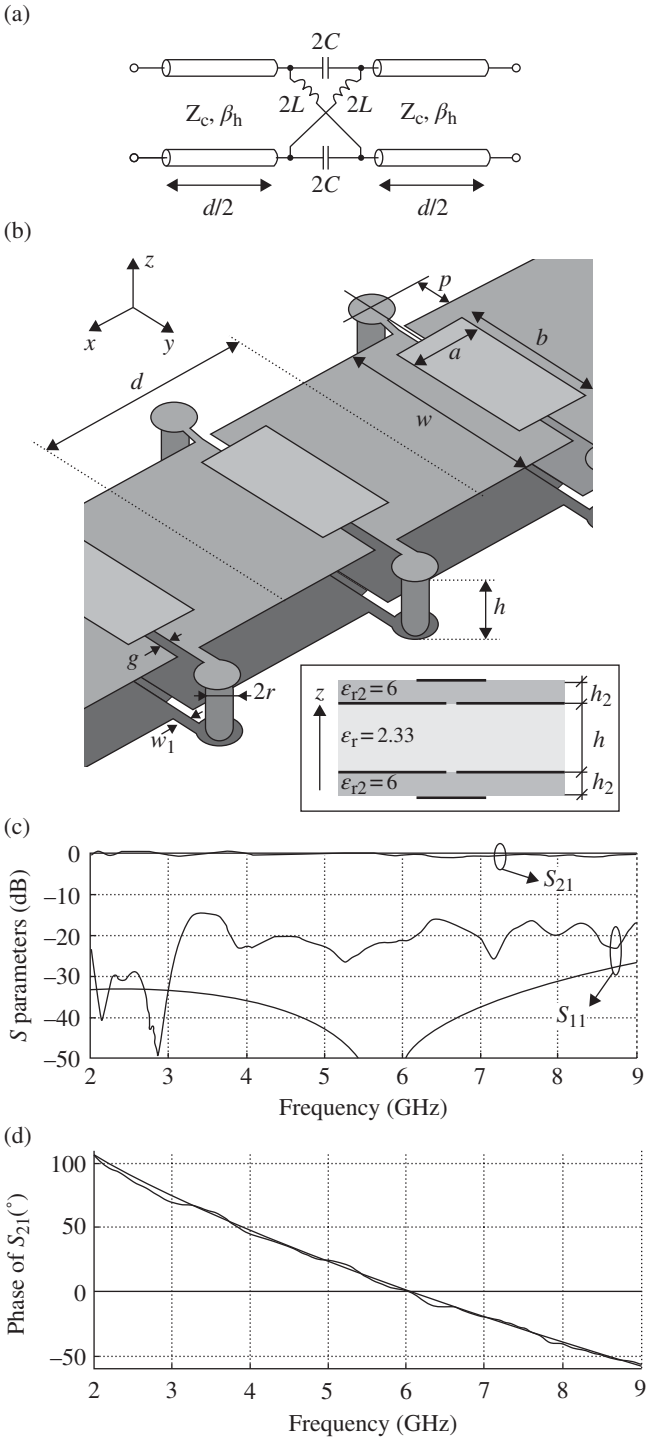


**FIGURE 6.28** Schematic (unit cell) (a), structure (b), S-parameters (c) and phase of $S_{21}$ (d) corresponding to a wideband CRLH transmission line implemented by means of X-type LH cells combined with transmission line sections. Reprinted with permission from Ref. [47]; copyright 2009 IEEE.

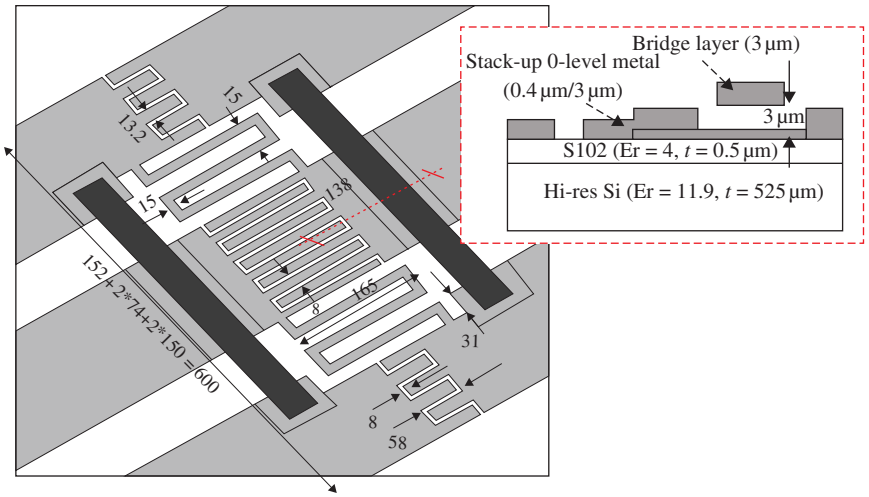


**FIGURE 6.29** Structure of the CRLH artificial transmission line based on a host CPW and X-type LH cells reported in Ref. [48]. Reprinted with permission from Ref. [48]; copyright 2011 IEEE.

implementation of lattice network-based artificial CRLH lines was presented in Ref. [43]. The unit cell is based on the coupled-microstrip Schiffman section [51], which is an easily implementable structure that does not require the use of via-holes or air bridges, as opposed to the cells presented in Refs. [45–49]. Indeed, coupled-line sections were earlier used in Refs [52, 53] to obtain CRLH transmission lines, but with limited performance due to the different even- and odd-mode phase velocities of the coupled lines. This issue was satisfactorily solved in [43]. Thus, terminated coupled line sections offer a simple approach for the implementation of lattice network CRLH transmission lines. Obviously, this is a fully distributed approach that inherently increases line size as compared to lattice network CRLH lines based on lumped or semilumped (planar) elements. The author recommends Refs [43, 50, 52, 53] to those readers interested on multiband CRLH lines based on coupled line sections.

***6.4.1.3 The Bridged-T Topology*** An interesting topology to achieve all-pass CRLH structures yet preserving the single-ended nature of the unit cell is the bridged-T (Fig. 6.30a). The equivalent T-circuit model of the bridged-T is depicted in Figure 6.30b. From it, the dispersion relation and characteristic impedance are found to be

$$\cos(\beta l) = \frac{2Z_1Z_2 + Z_2Z_3 + Z_1Z_3 + Z_1^2}{2Z_1Z_2 + Z_2Z_3 + Z_1^2} \tag{6.25}$$

$$Z_B = \frac{1}{2Z_1 + Z_3}\sqrt{Z_1^2Z_3^2 + 4Z_1^2Z_2Z_3 + 2Z_1Z_2Z_3^2 + 2Z_1^3Z_3} \tag{6.26}$$

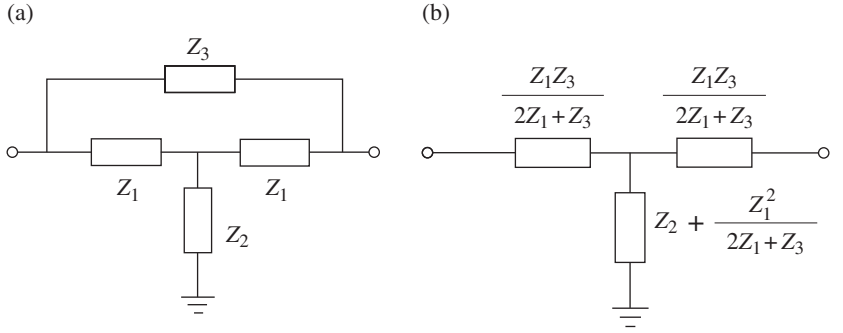


**FIGURE 6.30** Unit cell of the bridged-T network (a) and equivalent T-circuit model (b).

Depending on the specific impedances of the bridged-T network, the previous equations may lead to cumbersome expressions. However, notice that if the impedances satisfy

$$Z_3 = 4Z_2 \tag{6.27}$$

The dispersion relation and the characteristic impedance simplify to

$$\cos(\beta l) = 1 + \frac{2}{1 + \dfrac{2Z_2}{Z_1} + \dfrac{Z_1}{2Z_2}} \tag{6.28}$$

$$Z_B = \sqrt{2Z_1Z_2} \tag{6.29}$$

and the structure is all-pass provided the zeros and poles of $Z_1$ and $Y_2$ coincide (see Appendix I).

As an example, let us consider $Z_1 = 1/C\omega j$, $Z_2 = L\omega j$ and $Z_3 = 4Z_2$. With these impedances, the dispersion relation is

$$\cos(\beta l) = 1 + \frac{2}{1 - 2LC\omega^2 - \dfrac{1}{2LC\omega^2}} \tag{6.30}$$

This bridged-T network and the corresponding dispersion are depicted in Figure 6.31. The structure is all-pass and it exhibits forward wave propagation for frequencies below $\omega_o = (2LC)^{-1/2}$ and backward wave propagation above that frequency. Notice that if the signs of the reactances of $Z_1$ and $Z_2$ are interchanged and $Z_1 = 2L\omega j$ and $Z_2 = 1/2C\omega j$, the dispersion relation is also given by (6.30).

Higher-order (quad-band) all-pass bridged-T networks have been demonstrated and implemented by Ryan *et al*. [54] in microstrip technology. The reported structure

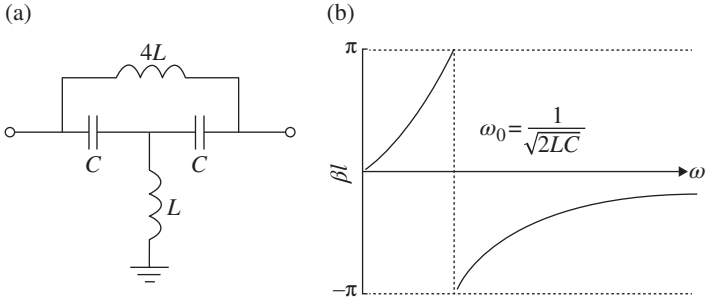


**FIGURE 6.31** Bridged-T network with $Z_1 = 1/C\omega j$ and $Z_2 = Z_3/4 = L\omega j$ (a), and dispersion diagram (b).

exhibits a very wide bandwidth of 1–8 GHz, thus confirming the potential of these single-ended structures for the realization of all-pass networks with CRLH characteristics.

### 6.4.2 Transmission Lines Based on Non-Foster Elements

In Chapter 3, it was shown that passive media with negative permeability and/or permittivity are intrinsically dispersive.[11] This means that it is not possible to synthesize single negative (SNG) or LH passive media exhibiting a constant (i.e., frequency independent) permeability and/or permittivity (it is well known that SNG and LH media are either described by the Drude or Lorentz models). In metamaterial transmission lines that can be modeled by an equivalent T- or π-circuit wave propagation is analogous to plane wave propagation in isotropic and homogeneous dielectrics (see the mapping Eqs.3.45 and 3.46 leading to an effective permittivity and permeability). Therefore, metamaterial transmission lines exhibiting backward wave propagation (including CRLH lines) must be also dispersive and hence bandwidth limited.[12]

In the previous subsection, it was shown that bandwidth can be enhanced by using lattice networks, which do not have an analogous to passive isotropic and homogeneous dielectrics. Another potential approach for bandwidth enhancement by minimizing dispersion is to use active components, or, more precisely, non-Foster elements. Non-Foster elements are reactive elements that do not obey the Foster reactance theorem [55].[13] Thus, the conditions $\partial\chi/\partial\omega > 0$ and $\partial B/\partial\omega > 0$ ($\chi$ and $B$ being reactance and susceptance, respectively) do not necessarily hold in such elements.

[11] Actually, passive plasma-like materials exhibiting positive permittivity and/or permeability satisfying $0 < \varepsilon < \varepsilon_o$ and/or $0 < \mu < \mu_o$ are also intrinsically dispersive (otherwise, expression (3.10) gives a density of energy smaller than the density of energy stored in vacuum). Such materials are usually designated as epsilon-near-zero (ENZ) and mu-near-zero (MNZ) metamaterials.

[12] Indeed bandwidth is also limited by the periodicity.

[13] The Foster theorem states that the reactance and susceptance of a passive, lossless two-terminal (one-port) network always monotonically increases with frequency.

This means that if a transmission line is implemented by means of non-Foster elements in the series and shunt branches, the effective permittivity and/or permeability of the line do not necessarily satisfy the conditions (3.12). Therefore, the design of dispersionless metamaterial transmission lines or artificial lines with engineered properties and small dispersion is potentially possible.

Negative inductances and capacitances are examples of non-Foster elements that can be implemented by means of negative impedance converters (NICs), that is, active electronic circuits [56].[14] In structures comprising such active components, the requirement of positive energy density (expression 3.11) no longer holds, and this leads also to violation of conditions (3.12). However, non-Foster elements may suffer from instability problems [57, 58]. For instance, let us consider a hypothetical transmission line consisting of a ladder network of series negative inductors and shunt negative capacitors. The effective permeability and permittivity of this line are simply given by (3.47) and (3.48). However, notice that the negative sign of the capacitance and inductance gives negative and constant values of the effective permittivity and permeability. In this structure, dispersion is only limited by periodicity (as occurs in the ladder network of a conventional transmission line). Indeed, the dispersion of this structure (derived from 2.33) is undistinguishable from the dispersion that results by considering positive element values. This result means that the phase and group velocities have the same sign in this line, which is in contradiction with LH wave propagation expected in structures with negative effective permittivity and permeability. This apparent contradiction is solved if one takes into account that such structure is unstable (under ordinary assumptions that both generator internal resistance and load resistance are positive), as it should occur in hypothetical materials with nondispersive negative parameters [57]. Notice also that, according to (3.6)–(3.9), stable backward wave propagation in LH media is guaranteed if the imaginary part of the effective permeability and permittivity are both negative (passive media), but these conditions are not necessarily satisfied in artificial materials with active inclusions.

According to the previous paragraph, instabilities might represent a limitation in non-Foster-based structures.[15] To the author knowledge, significant bandwidth enhancement in LH or CRLH lines by using non-Foster elements has not been experimentally demonstrated so far (nevertheless, theoretical and numerical investigations seem to confirm that broadband double-negative structures made of active inclusions are possible [59, 60]). However, very broadband ENZ transmission lines based on negative capacitances, exhibiting measured superluminal phase and group velocities over a broad band, have been reported [61, 62]. The principle for the implementation of such lines is simple: it consists of periodically loading a host transmission line with negative capacitors. The result is a fast-wave transmission line, as opposite to the

[14] The implementation of negative impedances through NICs is given in many textbooks and is out of the scope of this book.

[15] However, one should refrain from drawing a final conclusion about the feasibility of implementing dispersionless non-Foster-based structures, since the stability of transmission lines loaded with both ordinary "positive" elements and "negative" elements with gain is not well understood, and there are many effects that have not been studied so far.

slow-wave transmission lines studied in Chapter 2, that result by loading a host line with ordinary (positive) capacitors. As reported in Refs [61, 62], as long as the overall capacitance (i.e., the per-section capacitance of the line plus the negative capacitance) is positive, the structure is stable. Moreover, the designed and fabricated lines exhibit superluminal phase and group velocity in a very broad band since they were engineered to present a nondispersive (i.e., constant) effective permittivity smaller than the permittivity of vacuum (the effective permittivity can be made arbitrarily small by setting the absolute value of the negative capacitance close to the value of the line capacitance).

As pointed out in Refs. [61, 62], the superluminal group velocity is not related to the anomalous dispersion (a resonant narrowband phenomenon) that may arise in lossy media. On the contrary, the superluminal group (and phase) velocity in transmission lines loaded with negative capacitors is present in a very wide band, typically limited by the impossibility to generate the negative capacitance over a wide frequency band of the EM spectrum with practical NICs. However, as discussed in Ref. [62], and in many other sources, the fact that the group velocity is larger than $c$, the speed of light in vacuum, does not violate the theory of relativity and causality, since the group velocity is not identical to the energy velocity. The meaning of superluminal group velocity (and negative group velocity) is discussed in several papers (see, e.g., [63] and references therein, where this abnormal wave propagation phenomenon is reported). In brief, superluminal propagation means that the envelope of the wavepacket travels faster than $c$. However, this does not imply superluminal transmission of information, since under no circumstances the "front" velocity exceeds the speed of light in vacuum[16] (see Refs [61, 62] for further details).

To illustrate the potential of non-Foster elements for the implementation of broadband ENZ transmission lines, Figure 6.32 depicts the structure reported in Ref. [61], where a host line was loaded with three negative capacitors. The measured phase and group velocities, also depicted in Figure 6.32, indicate that superluminal propagation (with roughly frequency-independent phase and group velocity) is achieved in a very broad band (1:20). This means that the effective permittivity (real part) is nondispersive and smaller than the permittivity of vacuum in that band. Despite that the ENZ transmission line depicted in Figure 6.32 exhibits superluminal propagation at relatively small frequencies, the latest non-Foster ENZ transmission lines with superluminal phase and group velocities developed in the Group of Prof. Hrabar to date span the bandwidth 1MHz-400MHz (i.e., more than seven octaves) [64].

## 6.5 SUBSTRATE-INTEGRATED WAVEGUIDES AND THEIR APPLICATION TO METAMATERIAL TRANSMISSION LINES

Substrate-integrated waveguides (SIWs) are planar structures able to guide EM waves in a similar fashion to rectangular waveguides. In SIWs, the lateral metallic walls of the rectangular waveguides are replaced with a periodic array of metallic vias

[16] The carrying information "front" arises as long as any physically realizable signal is time limited; namely, any generated EM signal must have a beginning in time (i.e., a "front").

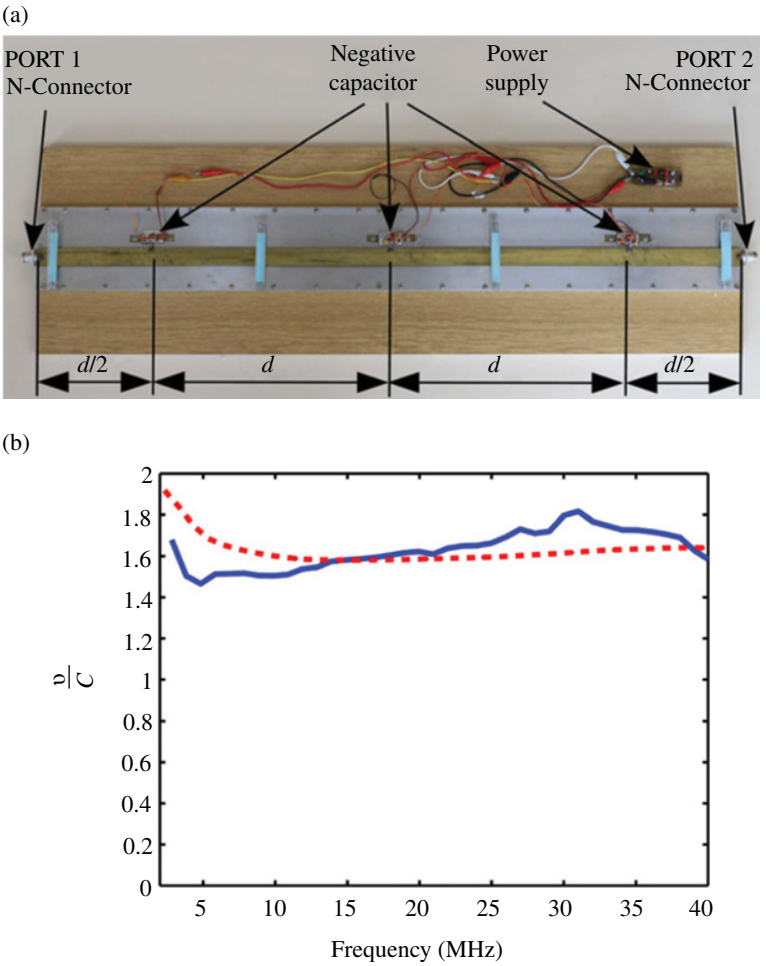


**FIGURE 6.32** Experimental realization of an ENZ transmission line operative in the 2–40 GHz frequency range (a) and measured phase (dashed line) and group (solid line) velocities (b). The negative capacitances (−60 pF) were implemented through NICs based on the ultra-high-speed operational amplifier *AD8099*. The host transmission line was designed to exhibit a characteristic impedance of 31.5 Ω, corresponding to a distributed capacitance of 106 pF/m. These values were chosen to achieve a distributed capacitance of 45 pF/m in the loaded line, corresponding to an equivalent dielectric constant of 0.3 and to a 50 Ω characteristic impedance. Reprinted with permission from Ref. [61]; copyright 2011 AIP.

(see Fig. 6.33). Hence, the fabrication of SIWs is fully compatible with planar technology, and the advantages of such technology (mainly low cost and easy integration) are combined with the well-known advantages of conventional rectangular waveguides, namely, high-$Q$ factor and high power capacity [65–67]. Thus, SIWs are promising candidates for a new generation of low-cost PCB interconnects for ultra

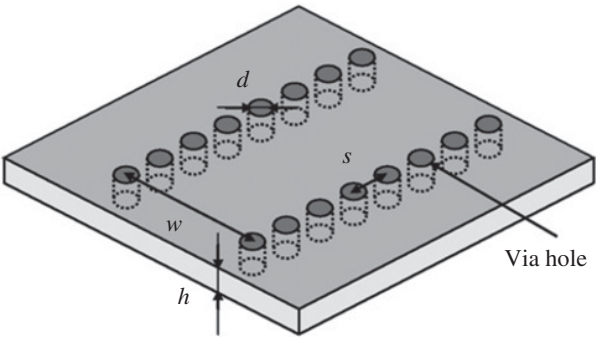


**FIGURE 6.33** Sketch of a SIW and its fundamental physical parameters. Reprinted with permission from Ref. [66]; copyright 2005 IEEE.

high-speed digital applications, and can also be used as building blocks for the implementation of microwave circuits (among them, those based on metamaterial concepts will be the ones considered in this section).

Essentially, SIWs emulate dielectric-filled rectangular waveguides whose lateral metallic walls are formed through rows of vias sufficiently close to each other. However, due to the absence of metal between adjacent vias, only $TE_{n0}$ modes are supported by SIWs[17] [66]. Indeed, the dispersion characteristics for these modes are the same as those of its equivalent rectangular waveguide [66]. Design formulas for the SIW, including the width, $W$ (essential to control the cutoff frequency of the dominant $TE_{10}$ mode), as well as limiting values of via diameter, $d$, and separation, $s$ (important to avoid radiation losses), can be found in Refs [66–68] and are summarized in the following:

$$W = 0.5\left[a + \sqrt{(a+0.54d)^2 - 0.4d^2}\right] + 0.27d \tag{6.31}$$

$$d \le \frac{2a}{5\sqrt{n^2-1}} \tag{6.32}$$

$$s \le 2d \tag{6.33}$$

where $a$ is the effective width of the SIW, related to the cutoff frequency of the $TE_{10}$ mode by:

$$a = \frac{c}{2f_{c10}\sqrt{\varepsilon_r}} \tag{6.34}$$

[17] Since TM modes impose longitudinal surface currents on the lateral walls of a rectangular waveguide, and considering that only vertical surface currents can flow in the SIW through the vertical metallic vias, such TM modes are not supported by SIWs. By the same reason, $TE_{nm}$ with $m$ not being equal to zero modes cannot be supported. Thus, only the $TE_{n0}$ modes can be preserved in SIWs.

$c$ and $\varepsilon_r$ being the speed of light in free space and the substrate dielectric constant, respectively. In (6.32), $n$ is the order of the first higher-order mode propagating along the SIW, which in turn determines the bandwidth of the fundamental $TE_{10}$ mode.[18] The previous formulas (6.31–6.34) are useful for design purposes, although they are empirical, and post optimization is typically required for both the SIW structure and the microstrip transitions, in order to satisfy design requirements (cutoff frequency, bandwidth, insertion and return losses, etc.) [68, 69].

There are many available papers that demonstrate the potential of SIWs for high-speed interconnects and planar microwave circuit design (some former examples of applications can be found in Ref. [70] and references therein). Indeed, SIWs can be considered to be a type of artificial transmission lines in the sense that their structure and functionality/performance are different than those of conventional lines. However, microwave circuit design using SIW technology is very similar to the design of waveguide-based circuits, and this is out of the scope of this book. Nonetheless, it has been demonstrated that by introducing further elements to SIWs, it is possible to implement artificial lines with functionalities similar to those of metamaterial transmission lines [71]. In particular, it is possible to implement CRLH lines and many circuits based on them, as well as planar filters/diplexers based on SIWs loaded with electrically small resonant elements (i.e., CSRRs). In the next subsections, these applications are briefly reviewed.

### 6.5.1 SIWs with Metamaterial Loading and Applications to Filters and Diplexers

Rectangular waveguides loaded with SRRs tuned below the cutoff frequency of the dominant TE mode and oriented perpendicularly to the magnetic field exhibit an LH pass band below that frequency [72]. Unfortunately, this configuration cannot be implemented in planar form by means of SIW technology due to the vertical orientation of the SRRs. Rectangular waveguides with CSRRs (and other complementary resonators) etched in the horizontal walls were used in Ref. [22] in order to experimentally obtain the resonance frequencies of such particles from the resulting notches in the transmission coefficient. In these experiments, the resonant elements were designed to exhibit the fundamental resonance frequency above the cutoff frequency of the waveguide. If an array of CSRRs is etched in the waveguide, it is expected that the structure exhibits a stopband behavior. Such stopband can be interpreted as due to the negative effective permittivity of the CSRRs (oriented perpendicular to the electric field). One advantage of CSRR-loaded rectangular waveguides (over SRR-loaded waveguides) is that the single vertically oriented metallic surfaces are the lateral walls of the waveguide. Therefore, it is apparent that by replacing such walls with metallic vias, CSRR-loaded SIWs exhibiting a stopband above cutoff will result. In CSRR-loaded microstrip lines, a similar stopband behavior is obtained.

[18] The microstrip transition plays an important role in determining the first higher-order mode propagating along the SIW (see Refs [68, 69] for further details), but this aspect is out of the scope of this book.

In order to switch the response to a pass band, series gaps are introduced in the strip of the microstrip line, and wave propagation in the first resulting pass band is backward. However, there is an alternative to obtain a pass band in CSRR-loaded microstrip lines, that is, to load the line with shunt inductive elements [73]. In this case, wave propagation is forward and occurs in the frequency region where the reactance of the shunt branch of the unit cell is capacitive (in such band, the CSRR array exhibits a positive permittivity that compensates the negative permittivity of the inductive elements).

In SIW technology, we can take advantage of the inherent negative permittivity below cutoff for the $TE_{10}$ mode (like in conventional rectangular waveguides). Thus, by tuning the resonance frequency of the CSRR below cutoff, a band pass behavior (with forward wave propagation) is expected. This has been corroborated and applied to the design of filters and diplexers in SIW technology [71, 74–76]. These filters are small as long as CSRR are electrically small resonators. As compared to CSRR-based filters in microstrip technology, the back substrate side is kept unaltered in these CSRR-loaded SIW filters. As an illustrative example, Figure 6.34 reports an order-3 bandpass filter first published in Ref. [74] (where the design methodology is explained in detail) and then included in the review paper [71]. An alternative approach considers the implementation of SIW filters by etching pairs of single loop CSRRs at both sides of the SIW (one on top of the other and rotated 180°) in a configuration that was designated as broadside coupled CSRR (BC-CSRR) by the authors [77].

### 6.5.2 CRLH Lines Implemented in SIW Technology and Applications

Let us now consider that the SIW is loaded with a transverse meandered slot on the top metallic surface, as depicted in Figure 6.35a [78, 79]. Such slot acts like a series capacitor. Since the SIW below cutoff behaves as a negative effective permittivity medium, and this behavior can be modeled by a shunt inductance, it follows that the circuit model of the unit cell of a slot-loaded SIW is the canonical CRLH transmission line model of Figure 3.20. Thus, backward and forward transmission bands are expected in slot-loaded SIWs, and wave propagation below cutoff is possible by properly tailoring the geometry. Obviously, by optimizing the structure, it is also possible to implement balanced CRLH lines.

Size reduction in SIWs can be achieved by simply cutting the structure by the longitudinal symmetry plane. The resulting structure is the so-called half-mode SIW (HM-SIW) [80, 81]. The field distribution in a HM-SIW for the dominant mode is very similar to that present in one of the halves of a conventional SIW. The reason is that the symmetric plane along the transmission direction is equivalent to a magnetic wall. Hence, half of the SIW will keep exactly the half field distribution unchanged if the cutting plane is a perfect magnetic wall. Actually, the open side aperture of the HM-SIW is nearly equivalent to a perfect magnetic wall due to the high ratio of width to height in the SIW. Thus, we can take benefit of this fact and implement SIWs with significantly reduced transverse dimensions, yet keeping the main properties of the original structure. The HM-SIW concept can also be applied to the implementation of CRLH structures based on transverse meandered slots. The typical unit cell of

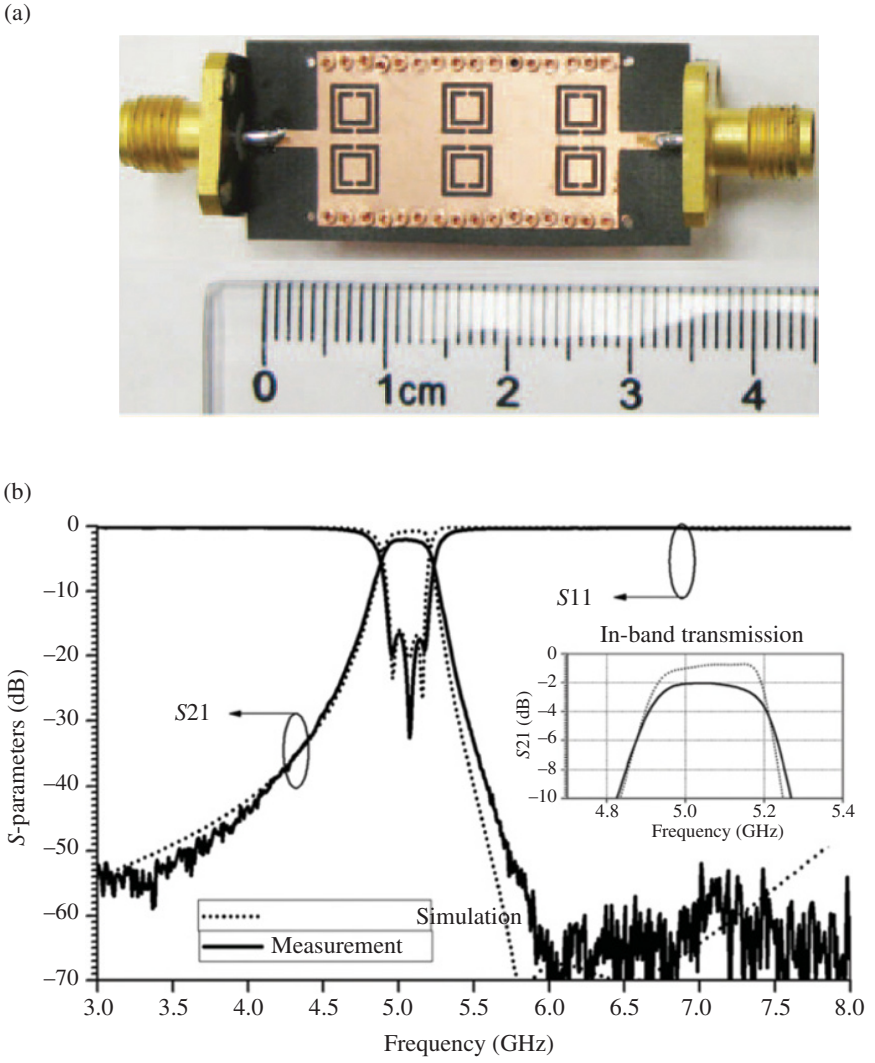


**FIGURE 6.34** Photograph (a) and frequency response (b) of a CSRR-loaded SIW designed to exhibit bandpass filter functionality. Reprinted with permission from Ref. [74]; copyright 2009 IEEE.

a CRLH HM-SIW transmission line is depicted in Figure 6.35b and c depicts a three-stage structure, including microstrip transitions [78].

In Ref. [78], it was demonstrated through simulation and experiment that CRLH SIW and their equivalent CRLH HM-SIW transmission lines roughly exhibit the same characteristics. Figure 6.36 depicts the dispersion diagrams and the frequency responses for the structure of Figure 6.35c by considering an unbalanced and a balanced case. As anticipated, the structures exhibit a CRLH behavior with a continuous

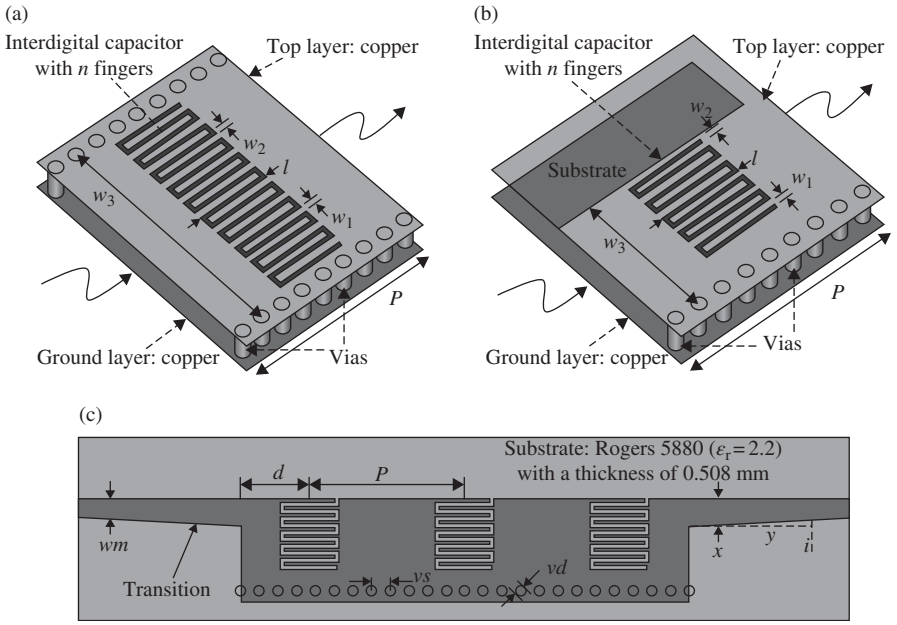


**FIGURE 6.35** Structure (unit cell) of a slot-loaded CRLH SIW (a), slot-loaded CRLH HM-SIW (b), and three-stage CRLH HM-SIW transmission line (c). Reprinted with permission from [78]; copyright 2009 IEEE.

transition between the LH and the RH band for the balanced case. The transmission coefficient of the SIW structure (without slot), also depicted in the figure, indicates that transmission below cutoff arises by introducing the slots.

CRLH SIW and CRLH HM-SIW transmission lines have been applied to the design of several microwave components, including couplers [78, 82], leaky wave antennas (LWAs) [79, 83], slot antennas [84], and so on. As an illustrative example, Figure 6.37 depicts a dual-band rat-race coupler based on CRLH HM-SIW lines [82], where the dual-band functionality is achieved thanks to the controllability of the dispersion diagram, as discussed in Subsection 4.2.2. The complete characterization of the device requires too many curves so that we include in Figure 6.37 the return loss, coupling, isolation, and phase balance by considering only the $\Delta$ port as the input port (the complete characterization and design process can be found in Ref. [82]). This approach is fully planar and does not require etching the back metallic side of the substrate.

Higher-order CRLH transmission lines implemented in SIW technology can also be implemented. In particular, order-4 CRLH SIW lines have been reported and applied to the design of quad-band splitters [85], dual-band filters [86], and dual-band LWAs [87]. Such lines were designated as extended CRLH (E-CRLH) SIW transmission lines in Refs [85–87]. A typical topology and equivalent circuit model of the proposed E-CRLH SIW transmission line unit cell is shown in Figure 6.38. The equivalent circuit is the canonical T-circuit of the E-CRLH transmission line basic cell with

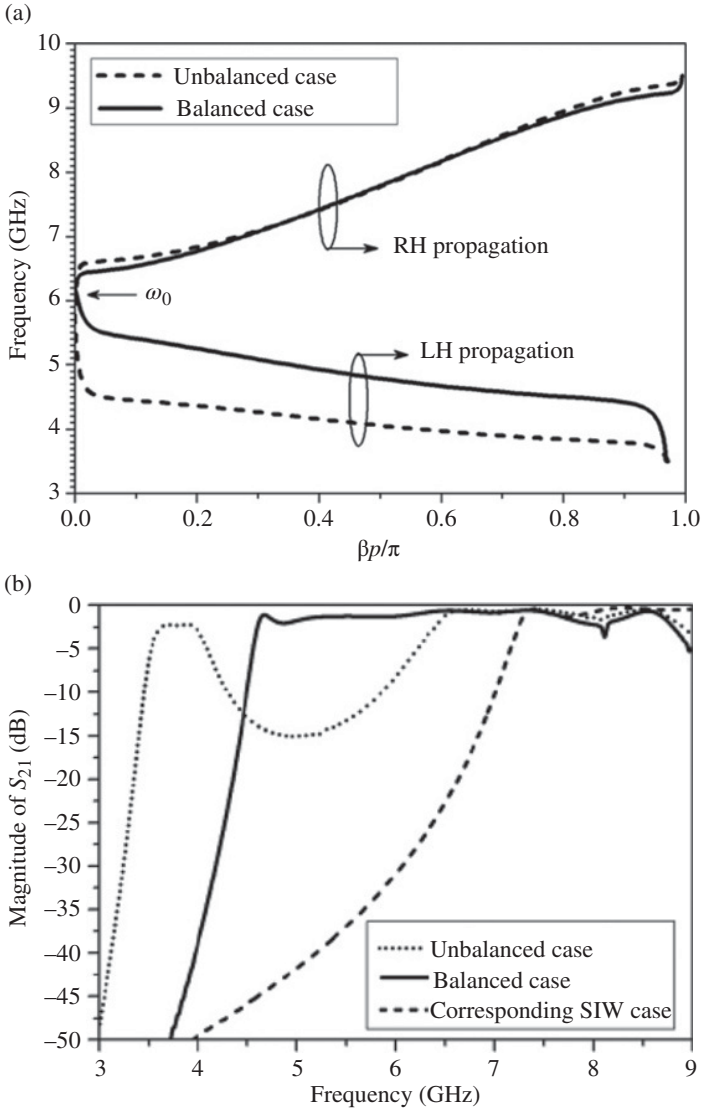


**FIGURE 6.36** Dispersion diagram (a) and response (b) of the CRLH SIW unit cells. Balanced case: $w_1 = 0.35$ mm, $w_2 = 0.33$ mm, $w_3 = 15$ mm, $n = 19$, $p = 12.5$ mm, and $l = 4.6$ mm. Unbalanced case: $w_1 = 0.35$ mm, $w_2 = 0.2$ mm, $w_3 = 15$ mm, $n = 19$, $p = 12.5$ mm, and $l = 4.8$ mm. The considered substrate is the *Rogers 5880* with thickness $h = 0.508$ mm and a relative permittivity $\varepsilon_r = 2.2$. All the metallic via holes have a diameter of 0.8 mm and a center-to-center spacing of 1.45 mm. Reprinted with permission from Ref. [78]; copyright 2009 IEEE.

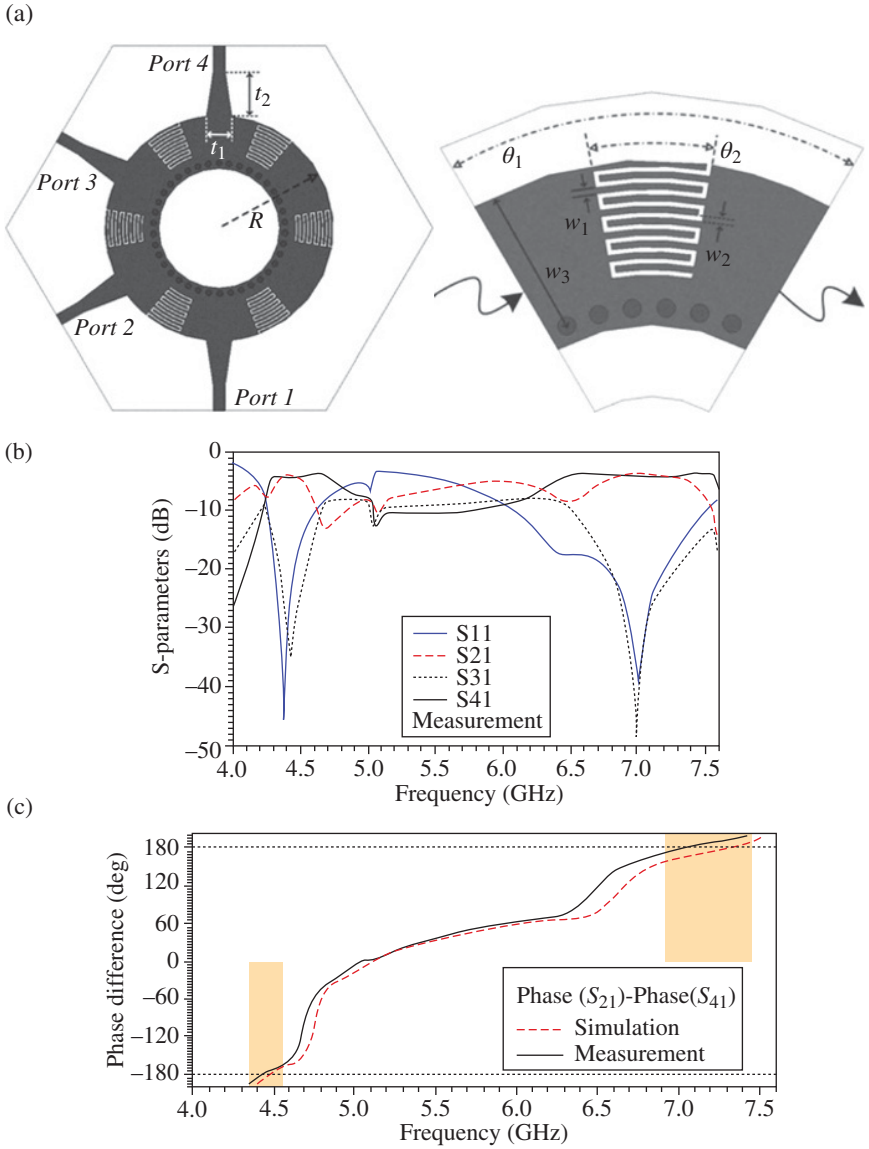


**FIGURE 6.37** Topology of the CRLH HM-SIW transmission line-based dual-band rat race coupler and detail of the unit cell (a), frequency response for the Δ port (b), and phase balance for the Δ port (c). The considered substrate is the *Rogers 5880* with a thickness $h = 0.508$ mm and a relative permittivity $\varepsilon_r = 2.2$. All the metallic via holes have a diameter of 0.8 mm and a center-to-center spacing of 1.45 mm. $w_1 = 0.3$ mm, $w_2 = 0.21$ mm, $w_3 = 6.55$ mm, $t_1 = 3.783$ mm, $t_2 = 7.04$ mm, $\theta_1 = 60°$, and $\theta_2 = 19.6°$. Reprinted with permission from Ref. [82]; copyright 2010 IEEE.

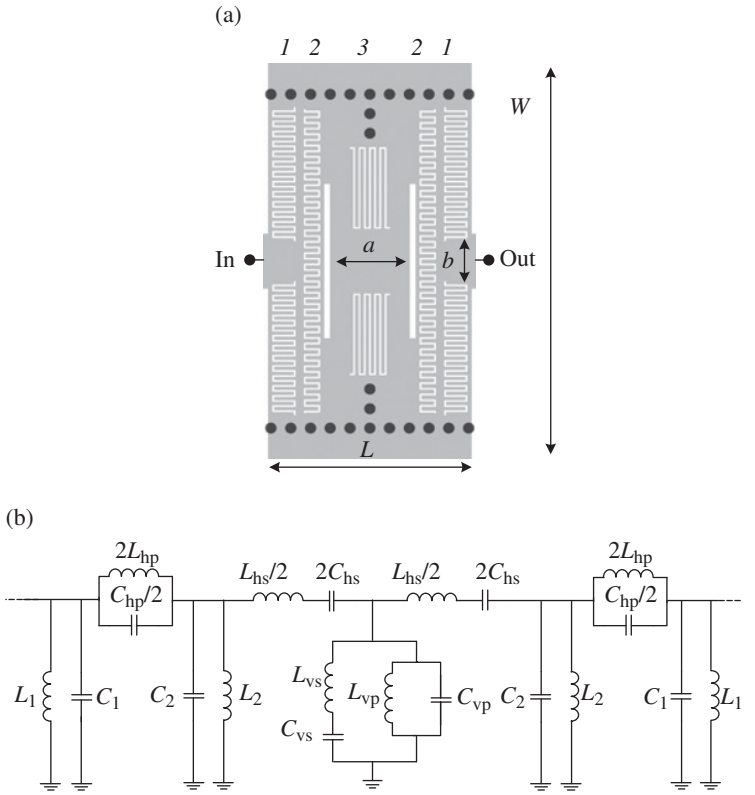


**FIGURE 6.38** Topology (a) and circuit model (b) of the SIW based E-CRLH transmission line. The top metal is indicated in gray, whereas the vias are indicated in black. Dimensions are $a = 5.66$ mm, $b = 3.34$ mm, $W = 28.34$ mm, and $L = 15.1$ mm. All the interdigital capacitors have a separation between fingers (gap) of 0.12 mm. The fingers width ($w_i$) and length ($l_i$) of the interdigital capacitors are for the series capacitors (from left to right): $w_1 = 0.24$ mm, $l_1 = 1.52$ mm and $w_2 = 0.285$ mm, $l_2 = 1.02$ mm; for the shunt branch, $w_3 = 0.25$ mm, and $l_3 = 5.72$ mm. The vertical slot has a width of 0.41 mm and length of 11.04 mm. The vias have a radius of 0.4 mm and a center-to-center distance between vias of 1.4 mm. Reprinted with permission from Ref. [85]; copyright 2012 EuMA.

additional shunt elements ($L_1$, $C_1$, $L_2$, $C_2$) to account for the distributed behavior of the SIW host line. The shunt capacitance and inductance $L_{vp} - C_{vp}$ are mainly determined by the SIW host line width $W$ and substrate thickness $h$. The series resonator $L_{hs} - C_{hs}$ models the etched series interdigital capacitors (labeled 2 in Fig. 6.38a). These element values can be controlled through the width and length of the fingers. By facing the same resonator to the grounded vias, the shunt $L_{vs} - C_{vs}$ series resonator is obtained (labeled 3). Moreover, considering this latter resonator the values $L_{vp} - C_{vp}$ can be further controlled by the vertical vias and length $a$. If the same series resonator with a central inductive path is added (controlled through the width $b$), a shunt

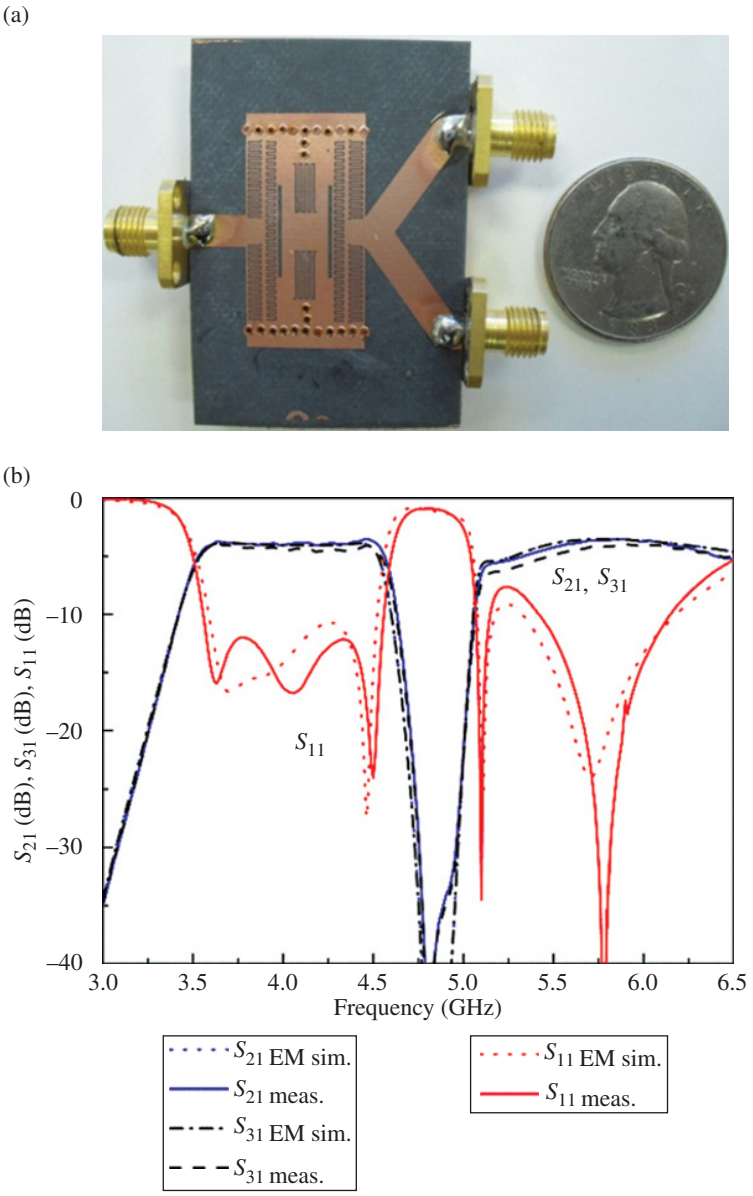


**FIGURE 6.39** Photograph (a) and frequency response (b) of the fabricated SIW quad-band Y-junction power divider based on the quad-band impedance inverter of Figure 6.38. Reprinted with permission from Ref. [85]; copyright 2012 EuMA.

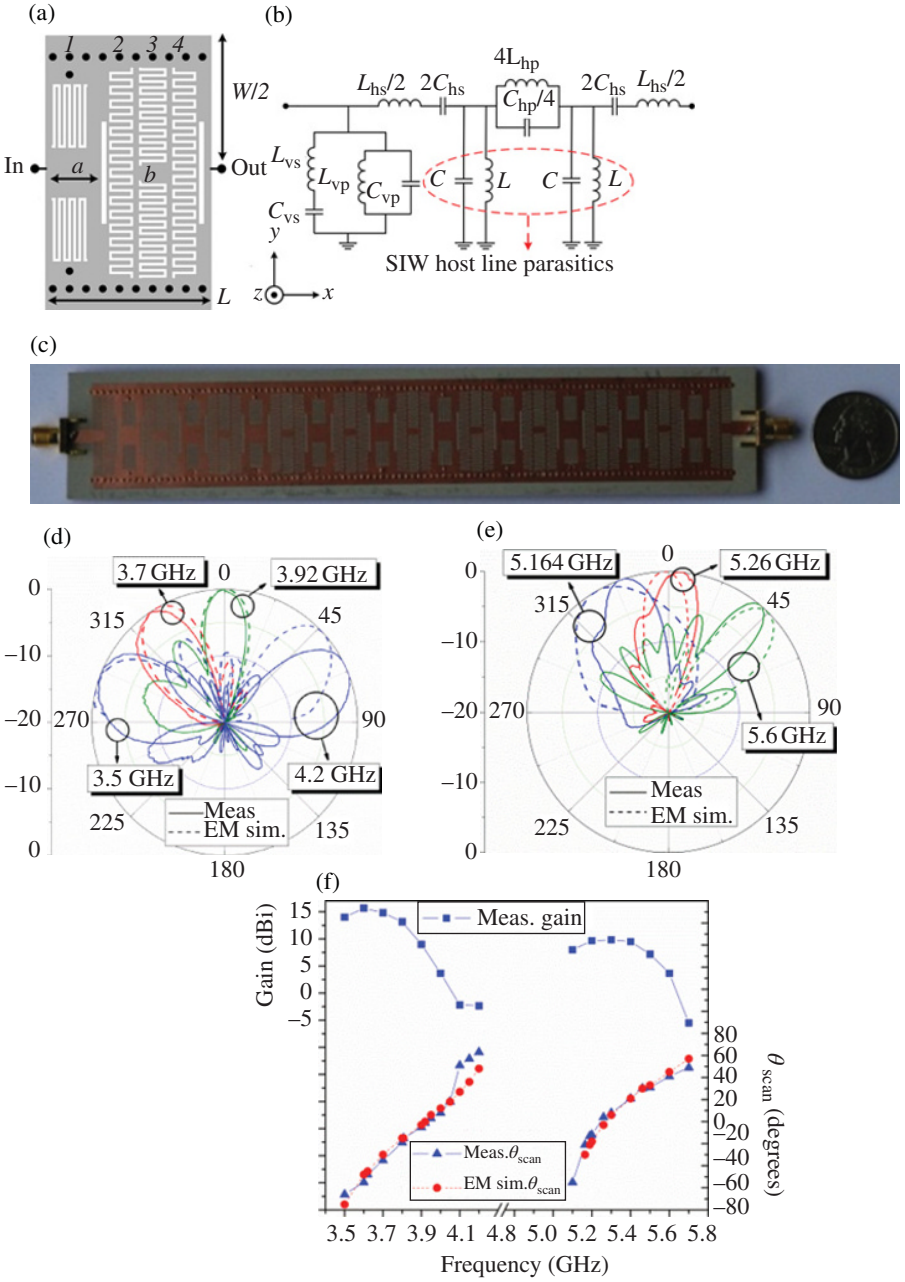


**FIGURE 6.40** Unit cell topology (a), circuit model (b), photograph (c), normalized radiation patterns ($x$–$z$ plane) for the first (d) and second (e) bands, and gain/scan angle (f) of the dual-band E-CRLH SIW LWA reported in Ref. [87]. Top numbers indicate the subindex

resonator in the series branch is obtained, corresponding to the $L_{hp} - C_{hp}$ resonator (labeled 1 in Fig. 6.38a). Finally, if increasing the series inductance $L_{hs}$ is required, additional slots adjacent to the series resonators can be etched (see Fig. 6.38a). This topology has a similar phenomenology as the canonical E-CRLH unit cell implemented in microstrip or CPW technology.

The topology of Figure 6.38 indeed corresponds to a designed quad-band 35.35 Ω impedance inverter, which was in turn used to implement a quad-band power splitter operative at 3.75 GHz, 4.46 GHz, 5.15 GHz and 5.9 GHz [85]. The fabricated device (implemented in the *Rogers 5880* substrate with dielectric constant $\varepsilon_r = 2.2$, thickness $h = 1.27$ mm, and loss tangent $\tan\delta = 0.001$) and its measured characteristics are depicted in Figure 6.39 [85] (device dimensions are given in the caption of Fig. 6.38). The design process and performance of this device are similar to those corresponding to quad-band inverters and dividers implemented by means of E-CRLH microstrip or CPW transmission lines. However, let us insist on the fact that the backside metal is not used for design purposes in the device of Figure 6.39.

The last example to illustrate the potential of E-CRLH SIW lines is a dual-band LWA, where continuous beam scanning with frequency from backward to forward leaky wave radiation is achieved in two predefined bands [87] (such CRLH dual-band LWAs were formerly proposed in microstrip technology [88]).[19] Figure 6.40 shows the photograph of the fabricated antenna, where the unit cell (also included) is similar to that depicted in Figure 6.38a, but described by the canonical L-type E-CRLH circuit model (except by the presence of the parasitics). The normalized radiation patterns, gains, and scan angles for different frequencies at both bands are also included in the figure (see Ref. [87] for further details on the design of this dual-band antenna).

In summary, the combination of SIW technology and metamaterial concepts is a powerful approach for the implementation of planar microwave components with novel functionalities, small size, low cost, low loss, and backside isolation.

---

**FIGURE 6.40** (*Continued*) for the dimensions of each interdigital capacitor. Dimensions are $a = 5.83$ mm, $b = 2.14$ mm, $W = 28.34$ mm, and $L = 17.2$ mm. The fingers width ($w_i$), length ($l_i$) and separation between fingers (gap $g_i$) of the interdigital capacitors are: for the shunt branch: $w_1 = 0.25$ mm, $g_1 = 0.28$ mm, $l_1 = 6$ mm; for the series capacitors (from left to right): $w_2 = w_4 = 0.45$ mm, $l_2 = l_4 = 1.94$ mm, $g_2 = g_4 = 0.26$ mm, $w_3 = 0.35$ mm, $l_3 = 2.3$ mm and $g_3 = 0.28$ mm; The vertical slot has a width of 0.5 mm and length of 10.49 mm. The vias have a radius of 0.4 mm and a horizontal and vertical center-to-center distance between vias of 1.72 mm and 1.84 mm, respectively. The considered substrate is the *Rogers RT/duroid 5880LZ* with permittivity $\varepsilon_r = 1.96$ and thickness $h = 1.27$ mm. Reprinted with permission from Ref. [87]; copyright 2013 IEEE.

[19] To achieve a continuous scan from backward to forward radiation at both bands, the E-CRLH SIW line must be balanced, that is, it must exhibit a continuous transition between the first LH band and the first RH band, and also a continuous transition between the second LH band and the second RH band.

## REFERENCES


1. E. Shamonina, V. A. Kalinin, K. H. Ringhofer, and L. Solymar, "Magneto-inductive waveguide," *Electron. Lett.*, vol. **38**, pp. 371–373, 2002.
2. E. Shamonina, V. A. Kalinin, K. H. Ringhofer, and L. Solymar, "Magneto-inductive waves in one, two and three dimensions," *J. Appl. Phys.*, vol. **92**, pp. 6252–6261, 2002.
3. M. C. K. Wiltshire, E. Shamonina, I. R. Young, and L. Solymar, "Dispersion characteristics of magneto-inductive waves: comparison between theory and experiment," *Electron. Lett.*, vol. **39**, pp. 215–217, 2003.
4. E. Shamonina and L. Solymar, "Properties of magnetically coupled metamaterial elements," *J. Magn. Magn. Mater.*, vol. **300**, pp. 38–43, 2006.
5. R. R. A. Syms, E. Shamonina, V. Kalinin, and L. Solymar, "A theory of metamaterials based on periodically loaded transmission lines: interaction between magnetoinductive and electromagnetic waves," *J. Appl. Phys.*, vol. **97**, paper 064909, 2005.
6. M. J. Freire, R. Marqués, F. Medina, M. A. G. Laso, and F. Martin, "Planar magnetoinductive wave transducers: theory and applications," *Appl. Phys. Lett.*, vol. **85**, pp. 4439–4441, 2004.
7. M. Beruete, F. Falcone, M. J. Freire, R. Marqués, and J. D. Baena, "Electroinductive waves in chains of complementary metamaterial elements," *Appl. Phys. Lett.*, vol. **88**, paper 083503, 2006.
8. J. Shefer, "Periodic cylinder arrays as transmission lines," *IEEE Trans. Microw. Theory Techn.*, vol. **11**, pp. 55–61, 1963.
9. E. Shamonina and L. Solymar, "Magneto-inductive waves supported by metamaterials elements: components for a one-dimensional waveguide," *J. Phys. D: Appl. Phys.*, vol. **37**, pp. 362–367, 2004.
10. I. S. Nefedov, and S. A. Tretyakov, "On potential applications of metamaterials for the design of broadband phase shifters," *Microw. Opt. Technol. Lett.*, vol. **45**, pp. 98–102, 2005.
11. F. J. Herraiz-Martínez, F. Paredes, G. Zamora, F. Martín, and J. Bonache, "Printed magnetoinductive-wave (MIW) delay lines for chipless RFID applications," *IEEE Trans. Antenna Propag.*, vol. **60**, pp. 5075–5082, 2012.
12. M. Schüßler, C. Damm, and R. Jakoby, "Periodically LC loaded lines for RFID backscatter applications," *1st Int. Congress. Adv. Electromagn. Mater. Microw. Opt. (Metamater.)*, Rome, Italy, October 2007, pp. 103–106.
13. M. Schüßler, C. Damm, M. Maasch, and R. Jakoby, "Performance evaluation of left-handed delay lines for RFID backscatter applications," *IEEE MTT-S Int. Microw. Symp. Dig*., Atlanta, GA, June 2008, pp. 177–180.
14. B. C. Tseng and L. K. Wu, "Design of miniaturized common-mode filter by multilayer low-temperature co-fired ceramic," *IEEE Trans. Electromagn. Compat.*, vol. **46**, pp. 571–579, 2004.
15. C.-H. Tsai and T.-L. Wu, "A broadband and miniaturized common-mode filter for gigahertz differential signals based on negative-permittivity metamaterials," *IEEE Trans. Microw. Theory Techn.*, vol. **58**, pp. 195–202, 2010.
16. W. T. Liu, C.-H. Tsai, T.-W. Han, and T.-L. Wu, "An embedded common-mode suppression filter for GHz differential signals using periodic defected ground plane," *IEEE Microw. Wireless Compon. Lett.*, vol. **18**, pp. 248–250, 2008.
17. S.-J. Wu, C.-H. Tsai, T.-L. Wu, and T. Itoh, "A novel wideband common-mode suppression filter for gigahertz differential signals using coupled patterned ground structure," *IEEE Trans. Microw. Theory Techn.*, vol. **57**, pp. 848–855, 2009.

18. J. Naqui, A. Fernández-Prieto, M. Durán-Sindreu, J. Selga, F. Medina, F. Mesa, and F. Martín, "Split rings-based differential transmission lines with common-mode suppression," *IEEE MTT-S Int. Microw. Symp. Dig*, Baltimore, MD, June 2011.
19. J. Naqui, A. Fernández-Prieto, M. Durán-Sindreu, F. Mesa, J. Martel, F. Medina, and F. Martín, "Common mode suppression in microstrip differential lines by means of complementary split ring resonators: theory and applications," *IEEE Trans. Microw. Theory Techn.*, vol. **60**, pp. 3023–3034, 2012.
20. A. Fernández-Prieto, J. Martel, J. S. Hong, F. Medina, S. Qian, and F. Mesa, "Differential transmission line for common-mode suppression using double side MIC technology," *Proc. 41st Eur. Microw. Conf. (EuMC)*, Manchester, UK, October 2011, pp. 631–634.
21. D. Ahn, J.-S. Park, C.-S. Kim, J. Kim, Y. Qian, and T. Itoh, "A design of the low-pass filter using the novel microstrip defected ground structure," *IEEE Trans. Microw. Theory Techn.*, vol. **49**, pp. 86–93, 2001.
22. J. D. Baena, J. Bonache, F. Martín, R. Marqués, F. Falcone, T. Lopetegi, M. A. G. Laso, J. García, I. Gil, and M. Sorolla, "Equivalent circuit models for split ring resonators and complementary split rings resonators coupled to planar transmission lines," *IEEE Trans. Microw. Theory Techn.*, vol. **53**, pp. 1451–1461, 2005.
23. J. Bonache, M. Gil, I. Gil, J. Garcia-García, and F. Martín, "On the electrical characteristics of complementary metamaterial resonators," *IEEE Microw. Wireless Compon. Lett.*, vol. **16**, pp. 543–545, 2006.
24. C. H. Wu, C. H. Wang, and C. H. Chen, "Novel balanced coupled-line bandpass filters with common-mode noise suppression," *IEEE Trans. Microw. Theory Techn.*, vol. **55**, pp. 287–295, 2007.
25. A. Saitou, K. P. Ahn, H. Aoki, K. Honjo, and K. Watanabe, "Differential-mode bandpass filters with four coupled lines embedded in self complementary antennas," *IEICE Trans. Electron.*, vol. **E90-C**, pp. 1524–1532, 2007.
26. C.-H. Wu, C.-H. Wang, and C. H. Chen, "Balanced coupled-resonator bandpass filters using multisection resonators for common-mode suppression and stopband extension," *IEEE Trans. Microw. Theory Techn.*, vol. **55**, pp. 1756–1763, 2007.
27. T. B. Lim and L. Zhu, "A differential-mode wideband bandpass filter on microstrip line for UWB applications," *IEEE Microw. Wireless Compon. Lett.*, vol. **19**, pp. 632–634, 2009.
28. J. Shi and Q. Xue, "Novel balanced dual-band bandpass filter using coupled stepped-impedance resonators," *IEEE Microw. Wireless Compon. Lett.*, vol. **20**, pp. 19–21, 2010.
29. J. Shi and Q. Xue, "Dual-band and wide-stopband single-band balanced bandpass filters with high selectivity and common-mode suppression," *IEEE Trans. Microw. Theory Techn.*, vol. **58**, pp. 2204–2212, 2010.
30. J. Shin and Q. Xue, "Balanced bandpass filters using center-loaded half-wavelength resonators," *IEEE Trans. Microw. Theory Techn.*, vol. **58**, pp. 970–977, 2010.
31. C.-H. Wu, C.-H. Wang, and C. H. Chen, "Stopband-extended balanced bandpass filter using coupled stepped-impedance resonators," *IEEE Microw. Wireless Compon. Lett.*, vol. **17**, pp. 507–509, 2007.
32. C.-H. Lee, C.-I. G. Hsu, and C.-C. Hsu, "Balanced dual-band BPF with stub-loaded SIRs for common-mode suppression," *IEEE Microw. Wireless Compon. Lett.*, vol. **20**, pp. 70–73, 2010.
33. X.-H. Wu and Q.-X. Chu, "Compact differential ultra-wideband bandpass filter with common-mode suppression," *IEEE Microw. Wireless Compon. Lett.*, vol. **22**, pp. 456–458, 2012.

34. P. Vélez, J. Naqui, A. Fernández-Prieto, M. Durán-Sindreu, J. Bonache, J. Martel, F. Medina, and F. Martín, "Differential bandpass filter with common mode suppression based on open split ring resonators and open complementary split ring resonators," *IEEE Microw. Wireless Compon. Lett.*, vol. **23**, pp. 22–24, 2013.
35. P. Vélez, J. Naqui, A. Fernánde Prieto, M. Durán-Sindreu, J. Bonache, J. Martel, F. Medina, and F. Martín, "Differential bandpass filters with common-mode suppression based on stepped impedance resonators (SIRs)," *IEEE MTT-S Int. Microw. Symp. Dig*., Seattle, WA, June 2013.
36. A. Fernandez-Prieto, J. Martel-Villagran, F. Medina, F. Mesa, S. Qian, J.-.S Hong, J. Naqui, and F. Martin, "Dual-band differential filter using broadband common-mode rejection artificial transmission line," *Prog. Electromagn. Res.*, vol. **139**, pp. 779–797, 2013.
37. J.-S. Hong and M. J. Lancaster, *Microstrip Filters for RF/Microwave Applications*, Wiley, Hoboken, NJ, 2001.
38. M. Durán-Sindreu, A. Vélez, F. Aznar, G. Sisó, J. Bonache, and F. Martín, "Application of open split ring resonators and open complementary split ring resonators to the synthesis of artificial transmission lines and microwave passive components," *IEEE Trans. Microw. Theory Techn.*, vol. **57**, pp. 3395–3403, 2009.
39. A. Velez, F. Aznar, J. Bonache, M.C. Velázquez-Ahumada, J. Martel, and F. Martín, "Open complementary split ring resonators (OCSRRs) and their application to wideband CPW band pass filters," *IEEE Microw. Wireless Compon. Lett.*, vol. **19**, pp. 197–199, 2009.
40. J. Naqui, M. Durán-Sindreu, J. Bonache, and F. Martín, "Implementation of shunt connected series resonators through stepped-impedance shunt stubs: analysis and limitations," *IET Microw. Antenna Propag.*, vol. **5**, pp. 1336–1342, 2011.
41. P. Vélez, M. Durán-Sindreu, A. Fernández-Prieto. J. Bonache, F. Medina, and F. Martín, "Compact dual-band differential power splitter with common-mode suppression and filtering capability based on differential-mode composite right/left handed transmission line metamaterials," *IEEE Ant. Wireless Propag. Lett.*, vol. **13**, pp. 536–539, 2014.
42. P. Vélez, J. Naqui, A. Fernández-Prieto, J. Bonache, J. Mata-Contreras, J. Martel, F. Medina, and F. Martín, "Ultra-compact (80 $mm^2$) differential-mode ultra-wideband (UWB) bandpass filters with common-mode noise suppression," *IEEE Trans. Microw. Theory Techn.*, vol. **63**, pp. 1272–1280, 2015.
43. J. Esteban, C. Camacho-Peñalosa, J. E. Page, and T. M. Martín-Guerrero, "Generalized lattice network-based balanced composite right-/left-handed transmission lines," *IEEE Trans. Microw. Theory Techn.*, vol. **60**, pp. 2385–2393, 2012.
44. O. J. Zobel, "Theory and design of uniform and composite electric wave filters," *Bell Syst. Technol. J.*, vol. **2**, pp. 1–46, 1923.
45. F. Bongard and J. R. Mosig, "A novel composite right/left-handed unit cell and potential antenna applications," *Proc. IEEE Antennas Propag. Soc. Int. Symp*., July 2008, pp. 1–4.
46. F. Bongard, J. Perruisseau-Carrier, and J. R. Mosig, "A novel composite right/left-handed unit cell based on a lattice topology: theory and applications," *2nd Int. Congr. Adv. Electromagn. Mater. Microw.Opt.* (*Metamater.*), Pamplona, Spain, September 2008, pp. 338–340.
47. F. Bongard, J. Perruisseau-Carrier, and J. R. Mosig, "Enhanced CRLH transmission line performances using a lattice network unit cell," *IEEE Microw. Wireless Compon. Lett.*, vol. **19**, pp. 431–433, 2009.

48. J. Perruisseau-Carrier, F. Bongard, M. Fernandez-Bolaños, and A. M. Ionescu, "A microfabricated 1-D metamaterial unit cell matched from DC to millimeter-waves," *IEEE Microw. Wireless Compon. Lett.*, vol. **21**, pp. 456–458, 2011.

49. P. Vélez, M. Durán-Sindreu, J. Bonache, and F. Martín, "Compact right-handed (RH) and left-handed (LH) lattice-network unit cells implemented in monolayer printed circuits," *Asia Pacific Microw. Conf.*, Melbourne, VIC, December 2011, pp. 534–537.

50. J. E. Page, J. Esteban, and C. Camacho-Peñalosa, "Lattice equivalent circuits of transmission-line and coupled-line sections," *IEEE Trans. Microw. Theory Techn.*, vol. **59**, pp. 2422–2430, 2011.

51. B. M. Schiffman, "A new class of broadband microwave 90-degree phase shifters," *IRE Trans. Microw. Theory Techn.*, vol. **MTT-6**, pp. 232–237, 1958.

52. A. M. E. Safwat, "Microstrip coupled line composite right/left-handed unit cell," *IEEE Microw. Wireless Compon. Lett.*, vol. **19**, pp. 434–436, 2009.

53. A. E. Fouda, A. M. E. Safwat, and H. El-Hennawy, "On the applications of the coupled-line composite right/left-handed unit cell," *IEEE Trans. Microw. Theory Techn.*, vol. **58**, pp. 1584–1591, 2010.

54. C. G. M. Ryan, and G. V. Eleftheriades, "A single-ended all-pass generalized negative-refractive-index transmission line using a bridged-T circuit," *IEEE-MTT-S Int. Microw. Symp. Dig*., Montreal, QC, June 2012.

55. R. M. Foster, "A reactance theorem," *Bell Syst. Technol. J.*, vol. **3**, no. 2, pp. 259–267, 1924.

56. J. G. Linvill, "Transistor negative-impedance converters," *Proc. IRE*, vol. **41**, pp. 725–729, 1953.

57. S. A. Tretyakov and S. I. Maslovski, "Veselago materials: what is possible and impossible about the dispersion of the constitutive parameters," *IEEE Antenna Propag. Mag.*, vol. **49**, pp. 37–43, 2007.

58. E. Ugarte-Muñoz, S. Hrabar, D. Segovia-Vargas, and A. Kiricenko, "Stability of non-Foster reactive elements for use in active metamaterials and antennas," *IEEE Trans. Antenna Propag.*, vol. **60**, pp. 3490–3494, 2012.

59. S. A. Tretyakov, "Meta-materials with wideband negative permittivity and permeability," *Microw. Opt. Technol. Lett.*, vol. **31**, pp. 163–165, 2001.

60. T. P. Weldon, K. Miehle, R. S. Adams, and K. Daneshva, "A wideband microwave double-negative metamaterial with non-Foster loading," *Proc. 2012 IEEE SoutheastCon*, Orlando, FL, March 2012.

61. S. Hrabar, I. Krois, I. Bonic, and A. Kiricenko, "Negative capacitor paves the way to ultra-broadband metamaterials," *Appl. Phys. Lett.*, vol. **99**, paper 254103, 2011.

62. S. Hrabar, I. Krois, I. Bonic, and A. Kiricenko, "Ultra-broadband simultaneous superluminal phase and group velocities in non-Foster epsilon-near-zero metamaterial," *Appl. Phys. Lett.*, vol. **102**, paper 054108, 2013.

63. M. Mojahedi, K. J. Malloy, G. V. Eleftheriades, J. Woodley, and R. Y. Chiao, "Abnormal wave propagation in passive media," *IEEE J. Sel. Top. Quant. Electron.*, vol. **9**, pp. 30–39, 2003.

64. S. Hrabar, I. Krois, I. Bonic, and A. Kiricenko, "Superluminal propagation in metamaterials: anomalous dispersion versus non-Foster approach," *7th Int. Congr. Adv. Electromagn. Mater. Microw. Opt. – Metamater. 2013*, Bordeaux, France, September 2013.

65. D. Deslandes and K. Wu, "Integrated microstrip and rectangular waveguide in planar form," *IEEE Microw. Wireless Compon. Lett.*, vol. **11**, pp. 68–70, 2001.

66. F. Xu and K. Wu, "Guided-wave and leakage characteristics of substrate integrated waveguide," *IEEE Trans. Microw. Theory Techn.*, vol. **53**, pp. 66–73, 2005.

67. D. Deslandes and K. Wu, "Design consideration and performance analysis of substrate integrated waveguide components," *Proc. Eur. Microw. Conf.*, Milan, Italy, September 2002, pp. 881–884.

68. J. E. Rayas-Sanchez and V. Gutierrez-Ayala, "A general EM-based design procedure for single-layer substrate integrated waveguide interconnects with microstrip transitions," *IEEE MTT-S Int. Microw. Symp. Dig.*, Atlanta, GA, June 2008.

69. J. E. Rayas-Sanchez, "An improved EM-based design procedure for single-layer substrate integrated waveguide interconnects with microstrip transitions," *IEEE MTT-S Int. Microw. Workshop Ser. Signal Integr. High-Speed Interconnects*, Guadalajara, Mexico, February 2009.

70. K. Wu, D. Deslandes, and Y. Cassivi, "The substrate integrated circuits—a new concept for high-frequency electronics and optoelectronics," *6th Int. Telecommun. Modern Satellite, Cable, Broadcast. Service. Conf.*, Nis, Serbia and Montenegro, October 2003, pp. P-III–P-X.

71. Y. Dong and T. Itoh, "Promising future of metamaterials," *IEEE Microw. Mag.*, vol. **13**, pp. 39–56, 2012.

72. R. Marques, J. Martel, F. Mesa, and F. Medina, "Left-handed-media simulation and transmission of EM waves in subwavelength split ring resonator-loaded metallic waveguides," *Phys. Rev. Lett.*, vol. **89**, pp. 183901–183904, 2002.

73. G. Sisó, M. Gil, J. Bonache, F. Martín, "Applications of resonant-type metamaterial transmission lines to the design of enhanced bandwidth components with compact dimensions," *Microw. Opt. Technol. Lett.*, vol. **50**, pp 127–134, 2008.

74. Y. Dong, T. Yang, and T. Itoh, "Substrate integrated waveguide loaded by complementary split-ring resonators and its applications to miniaturized waveguide filters," *IEEE Trans. Microw. Theory Techn.*, vol. **57**, pp. 2211–2223, 2009.

75. Y. Dong and T. Itoh, "Miniaturized dual-band substrate integrated waveguide filters using complementary split-ring resonators," *IEEE MTT-S Int. Microw. Symp. Dig*., Baltimore, MD, June 2011.

76. Y. Dong and T. Itoh, "Substrate integrated waveguide loaded by complementary split-ring resonators for miniaturized diplexer design," *IEEE Microw. Wireless Compon. Lett.*, vol. **21**, pp. 10–12, 2011.

77. L. Huang, I. D. Robertson, N. Yuan, and J. Huang, "Novel substrate integrated waveguide bandpass filter with broadside-coupled complementary split ring resonators," *IEEE MTT-S Int. Microw. Symp. Dig*., Montreal, QC, June 2012.

78. Y. Dong and T. Itoh, "Composite right/left-handed substrate integrated waveguide and half-mode substrate integrated waveguide," *IEEE MTT-S Int. Microw. Symp. Dig*., Boston, MA, June 2009, pp. 49–52.

79. Y. Dong and T. Itoh, "Composite right/left-handed substrate integrated waveguide and half mode substrate integrated waveguide leaky-wave structures," *IEEE Trans. Antenna Propag.*, vol. **59**, pp. 767–775, 2011.

80. W. Hong, B. Liu, Y. Q. Wang, Q. H. Lai, and K. Wu, "Half mode substrate integrated waveguide: a new guided wave structure for microwave and millimeter wave

application," *Proc. Joint 31st Int. Infrared Millimeter Waves Conf./14th Int. Terahertz Electron. Conf.*, Shanghai, China, September 2006, p. 219.

81. B. Liu, W. Hong, Y. Zhang, H. J. Tang, X. Yin, and K. Wu, "Half mode substrate integrated waveguide 180° 3-dB directional couplers," *IEEE Trans. Microw. Theory Techn.*, vol. **55**, pp. 2586–2592, 2007.
82. Y. Dong and T. Itoh, "Application of composite right/left-handed half-mode substrate integrated waveguide to the design of a dual band rat-race coupler," *IEEE MTT-S Int. Microw. Symp. Dig.*, Anaheim, CA, May 2010, pp. 712–715.
83. Y. Dong and T. Itoh, "Substrate integrated composite right-/left-handed leaky-wave structure for polarization-flexible antenna application," *IEEE Trans. Microw. Theory Techn.*, vol. **60**, pp. 760–771, 2012.
84. Y. Dong and T. Itoh, "Miniaturized substrate integrated waveguide slot antennas based on negative order resonance," *IEEE Trans. Antenna Propag.*, vol. **58**, pp. 3856–3864, 2010.
85. M. Durán-Sindreu, J. Bonache, F. Martín, and T. Itoh, "Novel fully-planar extended-composite right/left handed transmission line based on substrate integrated waveguide for multi-band applications," *Proc. Eur. Microw. Conf.*, Amsterdam, Netherlands, October 2012.
86. M. Durán-Sindreu, J. Bonache, F. Martín, and T. Itoh, "Single-layer fully-planar extended-composite right/left handed transmission lines based on substrate integrated waveguides for dual-band and quad-band applications," *Int. J. Microw. Wireless Technol.*, vol. **5**, pp. 213–229, 2013.
87. M. Durán-Sindreu, J. Choi, J. Bonache, F. Martín, and T. Itoh, "Dual-band leaky wave antenna with filtering capability based on extended-composite right/left-handed transmission lines," *IEEE MTT-S Int. Microw. Symp. Dig.*, Seattle, WA, June 2013.
88. C. G. M. Ryan and G. V. Eleftheriades, "A dual-band leaky-wave antenna based on generalized negative-refractive-index transmission-lines," *IEEE Antenna. Propag. Soc. Int. Symp. (APS-URSI)*, July 2010, pp. 1–4.